Available online at www.sciencedirect.com
ScienceDirect
Journal of Computational Physics 224 (2007) 1064–1094
JOURNAL OF COMPUTATIONAL PHYSICS
www.elsevier.com/locate/jcp

# Very high-order compact finite difference schemes on non-uniform grids for incompressible Navier–Stokes equations

Ratnesh K. Shukla, Mahidhar Tatineni, Xiaolin Zhong *

*Mechanical and Aerospace Engineering Department, University of California, 46-147C, Engineering IV Building, 420 Westwood Plaza, Los Angeles, CA 90095-1597, USA*

Received 27 January 2006; received in revised form 1 November 2006; accepted 6 November 2006
Available online 18 December 2006

**Abstract**

This article presents a family of very high-order non-uniform grid compact finite difference schemes with spatial orders of accuracy ranging from 4th to 20th for the incompressible Navier–Stokes equations. The high-order compact schemes on non-uniform grids developed in Shukla and Zhong [R.K. Shukla, X. Zhong, Derivation of high-order compact finite difference schemes for non-uniform grid using polynomial interpolation, J. Comput. Phys. 204 (2005) 404] for linear model equations are extended to the full Navier–Stokes equations in the vorticity and streamfunction formulation. Two methods for the solution of Helmholtz and Poisson equations using high-order compact schemes on non-uniform grids are developed. The schemes are constructed so that they maintain a high-order of accuracy not only in the interior but also at the boundary. Second-order semi-implicit temporal discretization is achieved through an implicit Backward Differentiation scheme for the linear viscous terms and an explicit Adam–Bashforth scheme for the non-linear convective terms. The boundary values of vorticity are determined using an influence matrix technique. The resulting discretized system with boundary closures of the same high-order as the interior is shown to be stable, when applied to the two-dimensional incompressible Navier–Stokes equations, provided enough grid points are clustered at the boundary. The resolution characteristics of the high-order compact finite difference schemes are illustrated through their application to the one-dimensional linear wave equation and the two-dimensional driven cavity flow. Comparisons with the benchmark solutions for the two-dimensional driven cavity flow, thermal convection in a square box and flow past an impulsively started cylinder show that the high-order compact schemes are stable and produce extremely accurate results on a stretched grid with more points clustered at the boundary.


*Keywords:* Compact schemes; High-order methods; Viscous incompressible flow

## 1. Introduction

Numerous techniques for the solution of viscous incompressible Navier–Stokes equations can generally be classified into two broad categories: global and local methods. Global methods encompass spectral and

* Corresponding author. Tel.: +1 310 825 2905.
*E-mail address:* xiaolin@seas.ucla.edu (X. Zhong).

0021-9991/$ - see front matter © 2006 Elsevier Inc. All rights reserved.
doi:10.1016/j.jcp.2006.11.007

pseudospectral methods which make use of the whole computational domain for the calculation of derivatives and quadrature formulas [1–3]. These methods have the advantage that they converge exponentially towards the exact solution as the number of modes is increased and hence have been very widely used in numerical calculations demanding high accuracy for a wide range of length scales, such as direct numerical simulation of turbulence. The main drawback of these methods is their inability to handle complicated boundary conditions and flow in complex geometries. Besides, clustering of collocation nodes at the boundary, in the case of Chebyshev spectral methods, also leads to very strict stability restrictions for long time integration [1,3,4]. Spectral element [5] and domain decomposition techniques have been quite successful in extending the applicability of spectral methods to some complicated flow problems. However, such methods are computationally expensive and are relatively difficult to implement. Unlike these global methods, local methods such as finite difference, finite volume and finite element methods compute the derivatives using neighboring nodes and are much more robust in handling complex boundary conditions and complicated geometries. The main disadvantage of these methods is their slow convergence towards the actual solution with grid refinement which necessitates use of many more grid points to achieve a desired accuracy level, when compared to global methods.

Compact higher order finite difference schemes [6–8] provide an effective way of combining the robustness of finite difference schemes and the accuracy of spectral methods. The computation of derivatives in compact finite differences is implicit in the sense that the derivative values at a particular node are computed not only from the function values but also from the values of the derivative at the neighboring nodes. Such an approach yields a global scheme without sacrificing the advantage of low computational cost and robustness of a scheme on a local stencil, since solution of the resulting multidiagonal sparse system can be carried out very efficiently. Compared to the finite difference schemes of the same order of accuracy, compact schemes utilize a smaller stencil and give better resolution especially at higher wavenumbers. Extensive study and discussion of the resolution characteristics of the higher order compact schemes on a uniform grid was carried out by Lele in [8]. Since then compact schemes have attained wide popularity in solving various problems involving incompressible and compressible flows [9–17]. In spite of this the application of higher order compact schemes has been restricted due to the instability of high-order boundary closures. An extensive review of the issues involving the instability of high-order boundary closures on uniform grids along with a discussion of the underlying concepts has been given in [18].

An alternative point of view adopted in [19–25] is to relate the instability associated with high-order boundary closures to the large oscillations of high-order interpolating polynomials (Runge phenomena) near the boundaries of a uniform grid. A Chebyshev interpolation polynomial utilizes crowding of collocation nodes at the boundary to suppress Runge phenomena. An extension of this idea to high-order compact schemes on non-uniform grid, with more grid points clustered at the boundary, was shown to yield stable boundary closures with the same order of accuracy as the interior [21]. Instead of using a grid transformation which remains susceptible to boundary instability an alternative route of deriving compact schemes from the interpolation polynomial was adopted in [21]. It was found that in accordance with the eigenvalue analysis, the computations for one and two-dimensional wave equations remained stable on a sufficiently stretched grid by suppressing oscillations due to Runge phenomena. The high-order schemes were subsequently applied to a two-dimensional linear convection diffusion equation in order to demonstrate their stability and accuracy. Note that the idea of using high-order interpolation polynomials has been utilized in [22–25] to develop a spectral finite volume method on unstructured grids. However, our present approach differs from these previous works utilizing high-order finite difference schemes on Chebyshev collocation nodes in that we use high-order compact schemes on a stretched non-uniform grid [4,21] which avoids the severe stability restrictions on time step size. In addition, our high-order compact schemes are constructed on a single domain, though in principle the idea can be extended to multiple domains.

The purpose of this paper is to extend the higher order compact schemes which were developed for linear model equations in [21] to incompressible Navier–Stokes equations in two dimensions. Compared to linear two-dimensional convection diffusion equation, the incompressible Navier–Stokes equations involve non-linear convective terms and an additional constraint of incompressibility. Hence, it is not clear if the high-order compact schemes on non-uniform grids, which are stable for linear wave and convection-diffusion equation, will maintain their stability and high accuracy for the incompressible Navier–Stokes equations. Previous investigations employing compact schemes for numerical solution of the Navier–Stokes equations have usually

been limited to orders of accuracy of four [9,10,12,15–17] and six [14]. In order to circumvent the problem of instability of high-order uniform compact schemes the accuracy of boundary closure schemes was lowered in [10]. Another approach is to use filtering in order to remove modes that are not resolved properly. However, filtering adds dissipation to the numerical scheme and this often results in a loss of sharp flow features in the computed solution [3]. In contrast to all these techniques, our aim in this work is to employ very high-order (4th–20th-order) collocated compact schemes to the incompressible Navier–Stokes equations without filtering. The overall order of the schemes is kept uniform throughout the computational domain by constructing boundary closure schemes which have the same order as the interior.

In this paper we are concerned with the two-dimensional incompressible driven cavity flow, convection in a differentially heated cavity with adiabatic top and bottom walls, and flow over an impulsively started cylinder. These problems have been widely used as test cases for the assessment and validation of numerical methods. Various different formulations that have been used successfully in the past to solve two-dimensional incompressible driven cavity problem include vorticity–streamfunction [29–33], velocity–pressure [27,28,36,38,39], vorticity–velocity [12,40–43], and pure streamfunction [15] formulation. The two most widely used techniques in order to handle the incompressibility constraint have been the fractional step approach and the influence matrix technique (cf. [1]). The influence matrix technique of Kleiser and Schumann [38] makes use of the principle of superposition for linear problems to compute a divergence free velocity field. This method has been used successfully in the past for the numerical solution in both the primitive variable [39] and the vorticity–streamfunction formulation [1]. The advantages and disadvantages of each formulation along with the issues involved in their implementation have been discussed in [37]. Due to its relative ease of implementation we use the vorticity–streamfunction formulation in our current work. However, in principle the schemes can be applied to the primitive variable formulation using either the influence matrix technique or the projection method for enforcing divergence free velocity field.

The paper is organized as follows: the details of the governing equations along with the desingularization technique employed to compute accurate numerical solutions are described in Section 2. The high-order compact schemes on non-uniform grids, with the same order for the boundary closures as for the interior schemes are described in Section 3. The temporal discretization scheme together with the influence matrix technique for computing the boundary values of vorticity, and Helmholtz/Poisson solver are described in Section 4. Results from numerical experiments showing the accuracy and stability of high-order compact schemes on a non-uniform grid with more grid points clustered at the boundary, when used to solve driven cavity flow, a convection benchmark problem and uniform flow past a circular cylinder, are presented in Section 5 before the conclusions.

## 2. Governing equations

### 2.1. Governing equations in vorticity–stream function formulation

We consider the incompressible Navier–Stokes equations for the unsteady two-dimensional flows in terms of the variables vorticity $\omega$ and stream function $\psi$ given by

$$\begin{aligned} &\frac{\partial \omega}{\partial t} + J(\omega,\psi) = \frac{1}{Re}\nabla^2\omega + \left(\frac{\partial f_y}{\partial x} - \frac{\partial f_x}{\partial y}\right), \\ &\nabla^2\psi = -\omega, \end{aligned} \tag{1}$$

along with appropriate initial and boundary conditions. Here, $J$ is the Jacobian with respect to the $x-y$ coordinates and represents the non-linear term:

$$J(\omega,\psi) = \mathbf{u}\cdot\nabla\omega = \frac{\partial \omega}{\partial x}\frac{\partial \psi}{\partial y} - \frac{\partial \omega}{\partial y}\frac{\partial \psi}{\partial x}. \tag{2}$$

$Re$ is the Reynolds number defined as $Re = UL/\nu$, with $U$, $L$ and $\nu$ representing a characteristic velocity, a characteristic length scale, and the kinematic viscosity, respectively, and $\mathbf{f} = [f_x, f_y]^T$ represents the forcing term. In this work we consider the numerical solution of (1) in a square domain $\Omega = [0,1]^2$ with the upper

lid sliding towards the right with a velocity $U_0(x)$ as shown in Fig. 1(a). The boundary conditions for the stream function $\psi$ are given by

$$\psi|_{\partial\Omega} = 0, \quad \left.\frac{\partial\psi}{\partial x}\right|_{x=0,1} = \left.\frac{\partial\psi}{\partial y}\right|_{y=0} = 0 \quad \text{and} \quad \left.\frac{\partial\psi}{\partial y}\right|_{y=1} = U_0(x), \tag{3}$$

where $\partial\Omega$ represents the boundary of $\Omega$. The Dirichlet boundary condition in (3) corresponds to the boundary being a constant streamline of value 0 whereas the Neumann boundary condition accounts for the no-slip condition at the cavity walls.

For the case of singular driven cavity flow, with $U_0(x) = -1$ and $\mathbf{f} = [0,0]^T$, one encounters singularities at the four corners of the domain. In particular the vorticity values at A(0, 1) and B(1, 1) are not finite due to the discontinuity in the boundary values of the horizontal velocity. A severe degradation in accuracy due to Gibb's phenomena was reported in [31] when the solution to this problem was obtained using a Galerkin-Legendre spectral method without any treatment of the singularities. Schultz et al. [35] obtained the solution to the Navier–Stokes equations by subtracting the Stokes contribution from the original singular problem. Botella and Peyret [27] obtained their benchmark spectral results for the singular driven cavity flow by subtracting the contribution of the first two singular terms, and using a projection method in $[\mathbf{u}, p]$ formulation. The effectiveness of the singularity subtraction technique was also demonstrated in the Legendre spectral computations of Auteri et al. [32] using an influence matrix technique in uncoupled vorticity–streamfunction formulation. Later, the technique was also employed in the Legendre spectral computations in [33] using a projection method in the primitive variables to investigate the stability of the singular driven cavity problem.

High-order compact schemes are global, like spectral methods, in that they use the whole computational domain for calculation of the derivatives. Due to this global nature of the high-order schemes we expect Gibb's oscillations to corrupt the numerical solutions obtained through the high-order compact schemes, unless proper treatment of singularities is performed. For this reason the singularity subtraction technique, for computing the numerical solutions to the singular driven cavity problem, is incorporated in our current work. Since the singularities at the corners C(1, 0) and D(0, 0) are weaker, following previous work only the singular contributions of the upper corners A and B are used in the computations.

### 2.2. Desingularization for the singular driven cavity problem

The details of the desingularization technique used for the singular driven cavity flow have been described in [27] and here we just outline the main ideas. The singular solutions to the corner flows at the points A and B

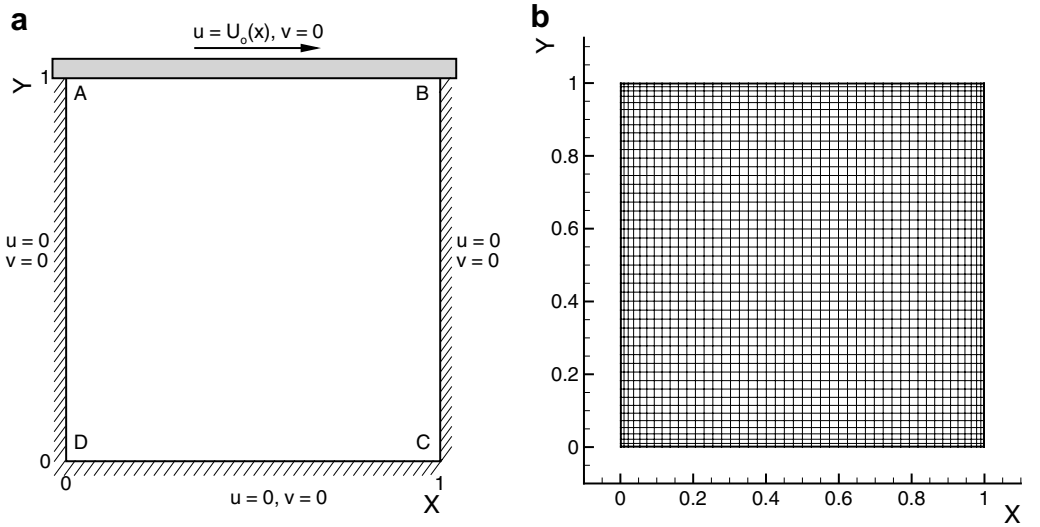


Fig. 1. (a) Schematic of the driven cavity problem showing the corners and the no-slip boundary conditions, and (b) a representative of the computational grid employed for the problem.

are obtained analytically in terms of expansion powers of $Re$ following the analysis for creeping flow by Batchelor [26], and its extension to flow at finite $Re$ by Gupta et al. in [34]. As in [27] only the first two terms are retained for the purpose of computations. The singular solution is then subtracted from the original governing equations in order to obtain a more regular problem in terms of perturbation variables $\tilde{\psi}$, $\tilde{\omega}$ as shown below

$$\frac{\partial\tilde{\omega}}{\partial t} + J(\tilde{\omega} + \omega^{S}_{Re}, \tilde{\psi} + \psi^{S}_{Re}) = \frac{1}{Re}\nabla^2\tilde{\omega} + \mathbf{u}^{A}_{0}\cdot\nabla\omega^{A}_{0} + \mathbf{u}^{B}_{0}\cdot\nabla\omega^{B}_{0}, \quad \nabla^2\tilde{\psi} = -\tilde{\omega}. \tag{4}$$

The boundary conditions on the perturbed streamfunction $\tilde{\psi}$ are given by

$$\begin{aligned}
&\tilde{\psi} = -(\psi^{A}_{Re} + \psi^{B}_{Re}), \quad \partial_y\tilde{\psi} = -\partial_y(\psi^{A}_{Re} + \psi^{B}_{Re}) = -(u^{A}_{Re} + u^{B}_{Re}) \quad \text{on } y = 0,\\
&\tilde{\psi} = 0, \quad \partial_y\tilde{\psi} = -1 \quad \text{on } y = 1,\\
&\tilde{\psi} = -\psi^{B}_{Re}, \quad \partial_x\tilde{\psi} = -\partial_x\psi^{B}_{Re} = v^{B}_{Re} \quad \text{on } x = 0,\\
&\tilde{\psi} = -\psi^{A}_{Re}, \quad \partial_x\tilde{\psi} = -\partial_x\psi^{A}_{Re} = v^{A}_{Re} \quad \text{on } x = 1,
\end{aligned} \tag{5}$$

where $\partial_x = \partial/\partial x$ and $\partial_y = \partial/\partial y$. The singular solutions used in the Eq. (5) are given by

$$\begin{aligned}
\mathbf{u}^{S}_{Re} &= \mathbf{u}^{A}_{Re} + \mathbf{u}^{B}_{Re} = (\mathbf{u}^{A}_{0} + \mathbf{u}^{B}_{0}) + Re(\mathbf{u}^{A}_{1} + \mathbf{u}^{B}_{1}),\\
\psi^{S}_{Re} &= \psi^{A}_{Re} + \psi^{B}_{Re} = (\psi^{A}_{0} + \psi^{B}_{0}) + Re(\psi^{A}_{1} + \psi^{B}_{1}),\\
\omega^{S}_{Re} &= \omega^{A}_{Re} + \omega^{B}_{Re} = (\omega^{A}_{0} + \omega^{B}_{0}) + Re(\omega^{A}_{1} + \omega^{B}_{1}).
\end{aligned} \tag{6}$$

In the above expressions the superscripts A and B stand for the singular solutions at the corners A and B, respectively, whereas the subscript $Re$ represents the total singular solution resulting from the contributions from both, the zeroth-order (Stokes) term, represented by the subscript 0, and, the first inertial term, represented by 1, of the series expansion in increasing powers of $Re$. For brevity detailed analytical expressions of the terms in the above equations are not reported and we refer the interested readers to Refs. [27,32].

## 3. Very high-order compact schemes on non-uniform grids

The numerical approximation of the governing Eq. (4), with the boundary conditions (5), is carried out on a computational grid such as the one shown in Fig. 1(b). The calculation of the first and the second derivatives in the spatial variables $x$ and $y$, for the convective and viscous terms, is accomplished through the application of the high-order compact schemes on a non-uniform grid. We employ the non-uniform grid compact schemes for the first and second derivatives derived in [21] for arbitrary orders of accuracy using polynomial interpolation. Throughout this paper the distribution of the grid points for $x \in [a,b]$ in one-dimension is taken to be [4]

$$x_i = \frac{b+a}{2} + (b-a)\frac{\sin^{-1}(-\alpha\cos(\pi i/N))}{2\sin^{-1}\alpha}, \quad i = 0,\ldots,N, \tag{7}$$

where the parameter $\alpha$ is used to change the stretching of the grid points from one limit of a Chebyshev grid at $\alpha \to 0$ to the other limit of a uniform grid at $\alpha = 1$. The grid spacing $h_i = x_i - x_{i-1}$ is defined as the distance between nodes $i$ and $i-1$. This distribution of grids has the advantage of forcing a stability restriction given by $O(N)$ as compared to $O(N^2)$ for Chebyshev collocation and thus avoids the severe time step restriction resulting from the CFL condition. The parameter $\alpha$ is a variable that can be chosen in order to satisfy the stability requirement arising from the eigenvalue analysis of the first derivative operator matrix, as described later in this section.

Next we describe the procedure for computing first and second derivatives using high-order compact schemes on non-uniform grid in moderate detail. Consider a function $u(x)$, $x \in [a,b]$, whose values $u_i$ are prescribed on the one-dimensional grid given by (7). The compact scheme discretizations relate the unknown vectors $U^{(1)}$ and $U^{(2)}$ composed of discrete first and second derivatives $u'_i$ and $u''_i$ to the vector $U$ composed of known discrete function values $u_i$ through relationships of the form

$$PU^{(1)} = QU, \quad \text{and} \quad \overline{P}U^{(2)} = \overline{Q}U, \tag{8}$$

where matrices $P$, $Q$, $\overline{P}$, $\overline{Q}$ are banded and are calculated using polynomial interpolation [21]. For example a fourth-order scheme, in both the interior and at the boundaries for the calculation of the $p$th derivative with $p = 1$ for the first derivative and 2 for the second is given by

$$\begin{aligned} &u_0^{(p)} + a_1 u_1^{(p)} = b_0 u_0 + b_1 u_1 + b_2 u_2 + b_3 u_3, \\ &a_{i-1} u_{i-1}^{(p)} + u_i^{(p)} + a_{i+1} u_{i+1}^{(p)} = b_{i-1} u_{i-1} + b_i u_i + b_{i+1} u_{i+1} \quad \text{for } 1 \leqslant i \leqslant N-1, \\ &a_{N-1} u_{N-1}^{(p)} + u_N^{(p)} = b_{N-3} u_{N-3} + b_{N-2} u_{N-2} + b_{N-1} u_{N-1} + b_N u_N, \end{aligned} \tag{9}$$

where the various coefficients have been tabulated in Table 1. At the boundary one-sided compact schemes are used in order to preserve tridiagonal matrices. The stencil width of the right hand side matrices $Q$ and $\overline{Q}$ are increased so that the boundary schemes have the same order as the interior. Throughout this paper, for convenience, we set the order of a scheme, for either the calculation of the first derivative or the second derivative, to be one less than the degree of the polynomial used for interpolation. It should be noted that a scheme which uses a particular stencil for the calculation of second derivative will actually be one order less accurate than a scheme using the same stencil for the calculation of the first derivative. The schemes constructed in this manner achieve maximum accuracy on a given stencil. Since the schemes are derived using polynomial interpolation they can be implemented for various orders of accuracy just by increasing the stencil width. It is also noted that explicit analytical expressions for the coefficients of a general compact scheme for the second derivative are available only for tridiagonal schemes and not for other multidiagonal schemes [21] and hence only tridiagonal compact schemes are used in the present work.

The value of parameter $\alpha$ in (7) determines the clustering of grid points near the boundary. In this work we choose $\alpha$ to be the maximum value for which the scheme yields only negative real eigenvalue components of the spatial first derivative operator matrix formed by removing the first row and column of $P^{-1}Q$ [21,20]. This is a necessary condition for the stability of the scheme when used for long time integration of a linear wave equation with fixed time varying boundary condition at one end [18]. The various values of maximum $\alpha$ that yield stable 16th-order and 20th-order schemes for various grid combinations that are used in the present work are listed in Table 2. The higher the order of a scheme, the more restrictive is the corresponding stability criteria and thus a value of $\alpha$ that makes a 16th-order scheme stable will give a stable scheme for lower orders of accuracy too. Note that the condition of existence of the second derivative schemes [21] is always found to be satisfied in each of the schemes for the non-uniform grid distributions listed in Table 2.

## 4. Discretization of incompressible Navier–Stokes equations

### 4.1. Time discretization

The temporal discretization of the governing Eq. (4) considered in the present work is semi-implicit and utilizes Adam–Bashforth explicit scheme for the non-linear Jacobian terms and second-order implicit Backward Differentiation scheme for the diffusion terms. The viscous term is treated implicitly in order to avoid the strong stability restriction. This combination of schemes has been widely used in obtaining incompressible flow solutions and is generally referred to as the AB/BDI2 scheme [1]. Since the smallest spatial scales are more difficult to resolve, when compared to the smallest temporal scales (cf. [44], this is a consequence of the stability restriction imposed by the CFL condition) it is reasonable to expect that a second-order accuracy in time will be sufficient for the present calculations. The time-discretized equations resulting from the application of the AB/BDI-2 scheme are given by

$$\begin{aligned} &(\nabla^2 - \gamma)\tilde{\omega}^{n+1} = S_\omega^{n,n-1} \quad \text{in } \Omega \\ &\nabla^2 \tilde{\psi}^{n+1} = -\tilde{\omega}^{n+1} \quad \text{in } \Omega, \end{aligned} \tag{10}$$

where

$$S_\omega^{n,n-1} = \frac{\gamma}{3}(\tilde{\omega}^{n-1} - 4\tilde{\omega}^n) + Re(2J(\tilde{\psi}^n + \psi_{Re}^S, \tilde{\omega}^n + \omega_{Re}^S) - J(\tilde{\psi}^{n-1} + \psi_{Re}^S, \tilde{\omega}^{n-1} + \omega_{Re}^S)), \tag{11}$$

Table 1
Coefficients of the fourth-order non-uniform grid compact scheme

| | $p=1$ | $p=2$ |
|---|---|---|
| $a_1$ | $\left\{\frac{(h_1+h_2)(h_1+h_2+h_3)}{h_2(h_2+h_3)}\right\}$ | $\left\{\frac{h_1(3h_1+4h_2+2h_3)+h_2(h_2+h_3)}{h_1(2h_2+h_3)-h_2(h_2+h_3)}\right\}$ |
| $b_0$ | $-\left\{\frac{2}{h_1}+\frac{1}{h_1+h_2}+\frac{1}{h_1+h_2+h_3}\right\}$ | $\left\{\frac{-6h_2^2-(4h_2+2h_3)(6h_1+3h_2+3h_3)}{(h_1+h_2)(h_1+h_2+h_3)(h_2(h_2+h_3)-h_1(2h_2+h_3))}\right\}$ |
| $b_1$ | $\left\{\frac{(h_2+h_1)(h_3+h_2+h_1)(2h_2^2+2h_2h_3-h_1h_3-2h_1h_2)}{h_1h_2^2(h_3+h_2)^2}\right\}$ | $\left\{\frac{6(h_1+h_2)^2+6(2h_1+2h_2+h_3)(h_2+h_3-h_1)}{h_2(h_2+h_3)(h_2(h_2+h_3)-h_1(2h_2+h_3))}\right\}$ |
| $b_2$ | $\left\{\frac{h_1^2(h_1+h_2+h_3)}{h_2^2h_3(h_1+h_2)}\right\}$ | $\left\{\frac{6h_1((h_2+h_3)^2+h_1(h_2+h_3)-h_1^2)}{h_2h_3(h_1+h_2)(h_1(2h_2+h_3)-h_2(h_2+h_3))}\right\}$ |
| $b_3$ | $\left\{\frac{h_1^2(h_1+h_2)}{(h_2+h_3)^2h_3(h_1+h_2+h_3)}\right\}$ | $\left\{\frac{6h_1(h_1h_2+h_2^2-h_1^2)}{h_2h_3(h_1+h_2)(h_1(2h_2+h_3)-h_2(h_2+h_3))}\right\}$ |
| $a_{i-1}$ | $\left\{\frac{h_{i+1}}{h_{i+1}+h_i}\right\}^2$ | $\left\{\frac{h_{i+1}}{h_i+h_{i+1}}\right\}\left\{\frac{h_i^2+h_ih_{i+1}-h_{i+1}^2}{h_i^2+3h_ih_{i+1}+h_{i+1}^2}\right\}$ |
| $a_{i+1}$ | $\left\{\frac{h_i}{h_{i+1}+h_i}\right\}^2$ | $\left\{\frac{h_i}{h_i+h_{i+1}}\right\}\left\{\frac{h_{i+1}^2+h_ih_{i+1}-h_i^2}{h_i^2+3h_ih_{i+1}+h_{i+1}^2}\right\}$ |
| $b_{i-1}$ | $-\left\{\frac{2h_{i+1}^2(2h_i+h_{i+1})}{h_i(h_{i+1}+h_i)^3}\right\}$ | $\left\{\frac{h_{i+1}}{h_i+h_{i+1}}\right\}\left\{\frac{12}{h_i^2+3h_ih_{i+1}+h_{i+1}^2}\right\}$ |
| $b_i$ | $\left\{\frac{2(h_{i+1}-h_i)}{h_ih_{i+1}}\right\}$ | $\left\{\frac{-12}{h_i^2+3h_ih_{i+1}+h_{i+1}^2}\right\}$ |
| $b_{i+1}$ | $\left\{\frac{2h_i^2(h_i+2h_{i+1})}{h_{i+1}(h_{i+1}+h_i)^3}\right\}$ | $\left\{\frac{h_i}{h_i+h_{i+1}}\right\}\left\{\frac{12}{h_i^2+3h_ih_{i+1}+h_{i+1}^2}\right\}$ |
| $a_N$ | $\left\{\frac{(\bar{h}_1+\bar{h}_2)(\bar{h}_1+\bar{h}_2+\bar{h}_3)}{\bar{h}_2(\bar{h}_2+\bar{h}_3)}\right\}$ | $\left\{\frac{\bar{h}_1(3\bar{h}_1+4\bar{h}_2+2\bar{h}_3)+\bar{h}_2(\bar{h}_2+\bar{h}_3)}{\bar{h}_1(2\bar{h}_2+\bar{h}_3)-\bar{h}_2(\bar{h}_2+\bar{h}_3)}\right\}$ |

Table 1 (*continued*)

| | $p=1$ | $p=2$ |
|---|---|---|
| $b_N$ | $-\left\{\frac{2}{\bar{h}_1}+\frac{1}{\bar{h}_1+\bar{h}_2}+\frac{1}{\bar{h}_1+\bar{h}_2+\bar{h}_3}\right\}$ | $\left\{\frac{-6\bar{h}_2^2-(4\bar{h}_2+2\bar{h}_3)(6\bar{h}_1+3\bar{h}_2+3\bar{h}_3)}{(\bar{h}_1+\bar{h}_2)(\bar{h}_1+\bar{h}_2+\bar{h}_3)(\bar{h}_2(\bar{h}_2+\bar{h}_3)-\bar{h}_1(2\bar{h}_2+\bar{h}_3))}\right\}$ |
| $b_{N-1}$ | $\left\{\frac{(\bar{h}_2+\bar{h}_1)(\bar{h}_3+\bar{h}_2+\bar{h}_1)(2\bar{h}_2^2+2\bar{h}_2\bar{h}_3-\bar{h}_1\bar{h}_3-2\bar{h}_1\bar{h}_2)}{\bar{h}_1\bar{h}_2^2(\bar{h}_3+\bar{h}_2)^2}\right\}$ | $\left\{\frac{6(\bar{h}_1+\bar{h}_2)^2+6(2\bar{h}_1+2\bar{h}_2+\bar{h}_3)(\bar{h}_2+\bar{h}_3-\bar{h}_1)}{\bar{h}_2(\bar{h}_2+\bar{h}_3)(\bar{h}_2(\bar{h}_2+\bar{h}_3)-\bar{h}_1(2\bar{h}_2+\bar{h}_3))}\right\}$ |
| $b_{N-2}$ | $\left\{\frac{\bar{h}_1^2(\bar{h}_1+\bar{h}_2+\bar{h}_3)}{\bar{h}_2^2\bar{h}_3(\bar{h}_1+\bar{h}_2)}\right\}$ | $\left\{\frac{6\bar{h}_1((\bar{h}_2+\bar{h}_3)^2+\bar{h}_1(\bar{h}_2+\bar{h}_3)-\bar{h}_1^2)}{\bar{h}_2\bar{h}_3(\bar{h}_1+\bar{h}_2)(\bar{h}_1(2\bar{h}_2+\bar{h}_3)-\bar{h}_2(\bar{h}_2+\bar{h}_3))}\right\}$ |
| $b_{N-3}$ | $\left\{\frac{\bar{h}_1^2(\bar{h}_1+\bar{h}_2)}{(\bar{h}_2+\bar{h}_3)^2\bar{h}_3(\bar{h}_1+\bar{h}_2+\bar{h}_3)}\right\}$ | $\left\{\frac{6\bar{h}_1(\bar{h}_1\bar{h}_2+\bar{h}_2^2-\bar{h}_1^2)}{\bar{h}_2\bar{h}_3(\bar{h}_1+\bar{h}_2)(\bar{h}_1(2\bar{h}_2+\bar{h}_3)-\bar{h}_2(\bar{h}_2+\bar{h}_3))}\right\}$ |

where $\bar{h}_1=-h_N$, $\bar{h}_2=-h_{N-1}$, $\bar{h}_3=-h_{N-2}$.

Table 2
Value of grid stretching parameter $\alpha$ for stable schemes

| Order | $N$ | | | | | | | | | |
|---|---|---|---|---|---|---|---|---|---|---|
| | 33 | 49 | 65 | 97 | 151 | 201 | 251 | 301 | 401 | 501 |
| 16 | 0.9 | 0.95 | 0.975 | 0.990 | 0.9960 | – | – | 0.9991 | – | – |
| 20 | – | – | – | 0.983 | 0.9931 | 0.9961 | 0.9975 | 0.9982 | 0.9990 | 0.9993 |

Only the values used in computations are reported.

and $\gamma = 3Re/2\Delta t$ with the boundary conditions on the perturbed streamfunction at time $n\Delta t$, $\tilde{\psi}^n$ given by (5). The superscript $n$ in the above equations denotes the time level at which the flow variables are being computed and it is noted that the expression for $S_\omega^{n,n-1}$, with $n>1$ involves terms already calculated at previous time steps $n$ and $n-1$. In order to keep the overall time stepping scheme second-order accurate, following [1], we use a starting scheme which extrapolates the solution obtained at the time instant $2\Delta t/3$ (computed by setting flow variables at $n=-1$ equal to those at $n=0$) to the solution at $\Delta t$ (corresponding to $n=1$), where $\Delta t$ is the time step size.

### 4.2. Spatial discretization

The spatial approximation of the time discretized Eq. (10) along with appropriate boundary conditions is achieved by the extension of the one dimensional compact differencing operators given by (8) to two dimensions. This leads to relationships of the form

$$\begin{aligned} P_1U_x &= Q_1U, \quad \overline{P}_1U_{xx} = \overline{Q}_1U, \\ U_yP_2^{\mathrm{T}} &= UQ_2^{\mathrm{T}}, \quad U_{yy}\overline{P}_2^{\mathrm{T}} = U\overline{Q}_2^{\mathrm{T}}, \end{aligned} \tag{12}$$

between the derivative matrices $U_x = [u_x(x_i, y_j)]$, $U_{xx} = [u_{xx}(x_i, y_j)]$, etc. and the function values $U = [u(x_i, y_j)]$, with $i = 0, \ldots, N_x$ and $j = 0, \ldots, N_y$ for a domain discretized using $(N_x + 1) \times (N_y + 1)$ grid points. Various matrices $P_1$, $Q_1$, etc. are banded as in one-dimension and are computed using polynomial interpolation. The distribution of grid nodes also involves a straightforward extension of the one-dimensional case (7) to two-dimensions and for a domain $\Omega = [0, 1]^2$ is given by

$$\begin{aligned} x_i &= \frac{1}{2} + \frac{\sin^{-1}(-\alpha_x \cos(\pi i/N_x))}{2 \sin^{-1} \alpha_x}, \quad i = 0, \ldots, N_x, \\ y_j &= \frac{1}{2} + \frac{\sin^{-1}(-\alpha_y \cos(\pi j/N_y))}{2 \sin^{-1} \alpha_y}, \quad j = 0, \ldots, N_y. \end{aligned} \tag{13}$$

The constants $\alpha_x$ and $\alpha_y$ control the amount of stretching in each direction and can be different in general. However, in the present work we only use a distribution of grid points that are equivalent in both $x$ and $y$ directions so that $\alpha_x = \alpha_y = \alpha$ and $N_x = N_y = N$. The parameter $\alpha$ is chosen according to the values listed in Table 2 so that the highest order scheme remains stable for the solution of a linear one-dimensional wave equation. The numerical solution of the semi-discrete Helmholtz and Poisson Eq. (10) is accomplished through an influence matrix technique and matrix-diagonalization method which are described in the following two sections.

### 4.3. Numerical approximation of Helmholtz equation

#### 4.3.1. Matrix-diagonalization method

In this section we describe the matrix-diagonalization method that is used to solve the algebraic system resulting from the high-order compact discretization of the Helmholtz equation with Dirichlet boundary conditions given by

$$\begin{aligned} &\nabla^2 u - \gamma u = f \quad \text{in } \Omega \\ &u = g \quad \text{on } \partial\Omega. \end{aligned} \tag{14}$$

As before, $\Omega = [0, 1]^2$ denotes a square domain with $\partial\Omega$ as its boundary. We follow the algorithm discussed in [1] in the context of spectral collocation method employing (12) for the spatial approximation of (14) on a non-uniform grid leading to

$$\overline{D}_1 \overline{U} + \overline{U} \overline{D}_2^{\mathrm{T}} - \gamma \overline{U} = F, \tag{15}$$

where $\overline{U}$ represents the matrix of unknowns in the interior points of the discretized domain

$$\Omega_N = (x_i, y_j), \quad i = 1, \ldots, N_x - 1, \ \ j = 1, \ldots N_y - 1. \tag{16}$$

The matrices $\overline{D}_1$ and $\overline{D}_2$ are computed as

$$\overline{D}_1 = \overline{P}_1^{-1} \overline{Q}_1, \quad \overline{D}_2 = \overline{P}_2^{-1} \overline{Q}_2, \tag{17}$$

with the dimensions reduced to $(N_x - 1) \times (N_x - 1)$ and $(N_y - 1) \times (N_y - 1)$ by removing the first and last columns and rows corresponding to the boundaries. The matrix $F$ is of dimensions $(N_x - 1) \times (N_y - 1)$ and is made up of $f$ and $g$. Next the matrices $\overline{D}_1$ and $\overline{D}_2$ are assumed to be diagonalizable and denoting the diagonal matrix whose entries are eigenvalues by $\Lambda_1$ and $\Lambda_2$ we obtain

$$\overline{D}_1 = R_1 \Lambda_1 R_1^{-1}, \quad \overline{D}_2 = R_2 \Lambda_2 R_2^{-1}, \tag{18}$$

where matrices $R_1$ and $R_2$ are formed by eigenvectors of $\overline{D}_1$ and $\overline{D}_2$. Using these relations (15) simplifies to

$$\Lambda_1 \widehat{U} + \widehat{U} \Lambda_2 - \gamma \widehat{U} = \widehat{F}, \tag{19}$$

where $\widehat{U} = R_1^{-1} \overline{U} (R_2^{\mathrm{T}})^{-1}$ and $\widehat{F} = R_1^{-1} \overline{F} (R_2^{\mathrm{T}})^{-1}$. The solution to (19) is immediately found as

$$\hat{u}_{i,j} = \frac{\hat{f}_{i,j}}{\lambda_{1,i} + \lambda_{2,j} - \gamma}, \quad i = 1, \ldots N_x - 1, \;\; j = 1, \ldots, N_y - 1, \tag{20}$$

where $\lambda_{1,i}$ and $\lambda_{2,j}$ are the eigenvalues of $\overline{D}_1$ and $\overline{D}_2$. Note that diagonalization of $\overline{D}_1$ and $\overline{D}_2$, in order to determine eigenvalues and eigenvectors, is carried out once for all at the preprocessing stage so that each solution of Helmholtz equation with Dirichlet boundary conditions involves only four matrix-matrix products which makes the calculations very efficient in terms of CPU usage. The method also assumes that the eigenvalues and eigenvectors resulting from diagonalization be purely real and non-zero and this is found to be the case in all the calculations involving high-order compact schemes on non-uniform grids listed in Table 2. However, computations involving high-order compact schemes on a uniform grid do give rise to eigenvalues which have both real and imaginary parts and in those cases we resort to an alternative method of solution described next.

*4.3.2. Direct solver*

In this section we describe an alternative technique for the solution of (14) discretized using the compact finite difference schemes on non-uniform grids given by (12) and (13). We first represent the discrete function at $(x_i, y_j)$ in the form of a vector of length $(N_x + 1) \times (N_y + 1)$ as

$$\mathbf{U} = [(u_{1,0}, u_{2,0}, \ldots, u_{N_x+1,0}), (u_{i,1}), \ldots, (u_{i,j}), \ldots, (u_{i,N_y+1})]^{\mathrm{T}}, \quad 0 \leqslant i \leqslant N_x + 1. \tag{21}$$

The discrete second derivative values $\mathbf{U}_{xx}$ and $\mathbf{U}_{yy}$, which are composed in a similar way, are related to $\mathbf{U}$ through following relationships:

$$\mathbf{A_1}\mathbf{U}_{xx} = \mathbf{B_1}\mathbf{U}, \quad \mathbf{A_2}\mathbf{U}_{yy} = \mathbf{B_2}\mathbf{U}. \tag{22}$$

The matrices $\mathbf{A_1}$, $\mathbf{A_2}$, $\mathbf{B_1}$, and $\mathbf{B_2}$ are sparse and are related to the second derivative matrices given by (12) as shown below

$$[\mathbf{A_1}] = \begin{bmatrix} [\overline{P}_1] & [0] & \ldots & [0] \\ [0] & [\overline{P}_1] & & \vdots \\ \vdots & \ddots & & \\ & & [\overline{P}_1] & [0] \\ [0] & \ldots & [0] & [\overline{P}_1] \end{bmatrix}, \quad [\mathbf{B_1}] = \begin{bmatrix} [\overline{Q}_1] & [0] & \ldots & [0] \\ [0] & [\overline{Q}_1] & & \vdots \\ \vdots & \ddots & & \\ & & [\overline{Q}_1] & [0] \\ [0] & \ldots & [0] & [\overline{Q}_1] \end{bmatrix},$$

$$[\mathbf{A_2}] = \begin{bmatrix} [I] & p_{0,1}[I] & \ldots & & & & [0] \\ p_{1,0}[I] & [I] & p_{1,2}[I] & & & & \cdot \\ [0] & \ldots & & & & \cdot & \\ \cdot & & \ldots & & & & \cdot \\ \cdot & & & \cdot & & & \cdot \\ \cdot & & & & \ldots & & [0] \\ \cdot & & & & p_{N_y-1,N_y-2}[I] & [I] & p_{N_y-1,N_y}[I] \\ [0] & \ldots & & & & p_{N_y,N_y-1}[I] & [I] \end{bmatrix}$$

In the above expression coefficients $p_{0,1}, p_{1,0}, \ldots, p_{N_y,N_y-1}$ correspond to the entries of the matrix $\overline{P}_2$. The matrix $\mathbf{B_2}$ has a similar form except that the bandwidth is increased with entries $p_{i,j}$ replaced by entries from the matrix $\overline{Q}_2$. Next, using the fact that matrices $\mathbf{A_1}$ and $\mathbf{A_2}$ commute (i.e. $\mathbf{A_1}\mathbf{A_2} = \mathbf{A_2}\mathbf{A_1}$), the discrete approximation to the Helmholtz equation is obtained as

$$(\mathbf{A_2}\mathbf{B_1} + \mathbf{A_1}\mathbf{B_2} - \gamma\mathbf{A_1}\mathbf{A_2})\mathbf{U} = \mathbf{A_1}\mathbf{A_2}\mathbf{F}, \tag{23}$$

where, the various matrices and known vector **F** are obtained after proper treatment of boundary conditions. A direct method based on the solution of this sparse system is implemented in the present work to obtain numerical results for computations on a uniform grid.

### 4.4. Influence matrix

The spatial discretization of the semi-discrete Eq. (10) using (12) yields

$$\begin{aligned} &(\nabla_{\mathrm{d}}^2-\gamma)\tilde{\omega}^n = S_{\omega}^{n,n-1} \quad \text{in } \Omega_N,\\ &\nabla_{\mathrm{d}}^2\tilde{\psi}^n = -\tilde{\omega}^n \quad \text{in } \Omega_N, \end{aligned} \tag{24}$$

with the boundary conditions

$$\begin{aligned} &\tilde{\psi}^n = -(\psi_{Re}^{\mathrm{A}}+\psi_{Re}^{\mathrm{B}}), \quad D_2\tilde{\psi}^n = -(u_{Re}^{\mathrm{A}}+u_{Re}^{\mathrm{B}}) \quad \text{on } y=0,\\ &\tilde{\psi}^n = 0, \quad D_2\tilde{\psi}^n = -1 \quad \text{on } y=1,\\ &\tilde{\psi}^n = -\psi^{\mathrm{B}}, \quad D_1\tilde{\psi}^n = v_{Re}^{\mathrm{B}} \quad \text{on } x=0,\\ &\tilde{\psi}^n = -\psi^{\mathrm{A}}, \quad D_1\tilde{\psi}^n = v_{Re}^{\mathrm{A}} \quad \text{on } x=1, \end{aligned} \tag{25}$$

where $D_1 = P_1^{-1}Q_1$ and $D_2 = P_2^{-1}Q_2$, and $\nabla_{\mathrm{d}}^2$ is the discrete high-order compact approximation for the Laplace operator. To solve the equation for $\tilde{\omega}^n$, boundary conditions on $\tilde{\omega}^n$ are required, which are obtained using an influence matrix technique. The details of the implementation of the influence matrix technique for a spectral Chebyshev collocation method are described in [1] and here we follow the same approach. The basic idea behind the method is to use the principle of superposition of solutions for the linear Eq. (24) by constructing a set of elementary solutions in the preprocessing stage and using them to compute the influence matrix. This influence matrix is then used at each time step to compute boundary values of vorticity. In order to compute the influence matrix the following problems are solved for $(\overline{\omega}_l, \overline{\psi}_l), l = 1, \ldots, 2(N_x+N_y-2)$ at the beginning of the computations,

$$\begin{aligned} &(\nabla_{\mathrm{d}}^2-\gamma)\overline{\omega}_l = 0 \quad \text{in } \Omega_N,\\ &\nabla_{\mathrm{d}}^2\overline{\psi}_l = -\overline{\omega}_l \quad \text{in } \Omega_N,\\ &\overline{\omega}_l|_{\eta_m} = \delta_{m,l} \quad \text{for } \eta_m \in \partial\Omega_N^I,\\ &\overline{\psi}_l|_{\eta_m} = 0 \quad \text{for } \eta_m \in \partial\Omega_N^I, \end{aligned} \tag{26}$$

where $\delta_{m,l}$ is the Kronecker delta. The discrete points $\partial\Omega_N^I$ in (26) denote the set of grid points on the boundary $\partial\Omega$ except for the corners A, B, C and D, and $\eta_m$, $m = 1, \ldots, 2(N_x+N_y-2)$ refer to the grid points on $\partial\Omega_N^I$. The influence matrix $M$ is then constructed as $M_{i,j} = D_n\overline{\psi}_l|_{\eta_j}$, where $D_n$ ($\approx\partial/\partial n$) denotes discrete normal derivative operator matrix and can be $D_1$ or $D_2$ depending on the boundary. The influence matrix $M$ found in this way has four null eigenvalues. The reason for this has been analyzed in [29]. Here the same method as in [29] is used to alleviate the problem which involves removal of four points on the boundary given by

$$P_1 = (x_1, 0), \quad P_2 = (x_{N_x-1}, 0), \quad P_3 = (x_1, 1), \quad \text{and} \quad P_4 = (x_{N_x-1}, 1). \tag{27}$$

With the influence matrix in place Eq. (24) are solved at each time step by first assuming zero boundary conditions on vorticity and Dirichlet boundary conditions on the streamfunction given by (25). We denote the solution so obtained by $(\hat{\psi}^n, \hat{\omega}^n)$ and construct a vector $\Phi$ of length $2(N_x+N_y-4)$ given by $D_n\tilde{\psi}^n - D_n\hat{\psi}^n$ on the boundary excluding corners and points $P_1$, $P_2$, $P_3$, and $P_4$, where subscript $n$ denotes normal and superscript $n$ denotes time level. The boundary values of vorticity are then computed using $M^{-1}\Phi$, and are used to compute actual vorticity field in the interior. Note that the boundary values of vorticity at the four corners and the removed points are set equal to 0. The streamfunction can then be recovered by solving the Poisson equation for $\tilde{\psi}^n$.

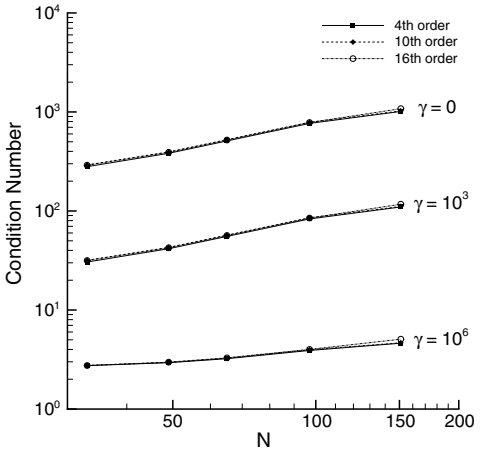


Fig. 2. Condition number of the influence matrix for various high-order compact schemes on non-uniform grids.

The efficiency of this method depends on the condition number of the influence matrix. Fig. 2 shows the variation of the condition number of the influence matrix $M$ computed numerically for non-uniform grid (13) with various amounts of grid points, stretching parameters taken from Table 2, and different choices of $\gamma$ using various high-order compact schemes. It is observed that the influence matrix is relatively well conditioned with the condition number almost the same for all the high-order compact schemes. This shows that the matrix $M$ can be inverted without significant loss of accuracy. We note that the actual values of the vorticity at the boundary have to be computed using $\tilde{\psi} = -\nabla^2\tilde{\omega}^n$ as in [29].

## 5. Numerical results

### 5.1. One-dimensional wave equation

In order to study the resolution characteristics of the high-order compact finite difference schemes on non-uniform grids we solve the one-dimensional wave equation

$$\frac{\partial u}{\partial t} + \frac{\partial u}{\partial x} = 0, \quad 0 \leqslant x \leqslant 1 \tag{28}$$

with initial and boundary conditions given by

$$u(x,0) = \sin(\omega\pi x), \quad u(0,t) = -\sin(\omega\pi t), \tag{29}$$

for various values of wavenumber $\omega$. As shown in [21], the high-order schemes are stable for the wave equation computations only if the grid stretching parameter $\alpha$ is prescribed in accordance with the eigenvalue analysis (Table 2). The Fourier analysis of the resolution characteristics of the high-order non-uniform grid compact schemes was presented in [21]. However, such an analysis assumes periodic boundary conditions and our aim here is to analyze the resolution properties of schemes when they are applied to solve the non-periodic problem defined by (28) and (29).

Runs are made for a range of values of wavenumber, $\omega$, using high-order compact schemes with even orders of accuracy ranging from four to 16 on a fixed number of grid points, $N = 49$. The values of $\omega$ are chosen such that the computational domain is not a multiple of the wavelength. The value of the grid stretching parameter $\alpha$ is set equal to 0.95 to ensure that the stability requirement of the highest order scheme (16th-order) is satisfied. A 4th-order explicit Runge–Kutta scheme is used for temporal time marching with the time step size chosen small enough so that the temporal discretization errors are negligible compared to those due to spatial discretization. Refinements in the time step size are used to ensure that the computed solutions are independent of time step size and the solutions are advanced in time for more than 50 periods.

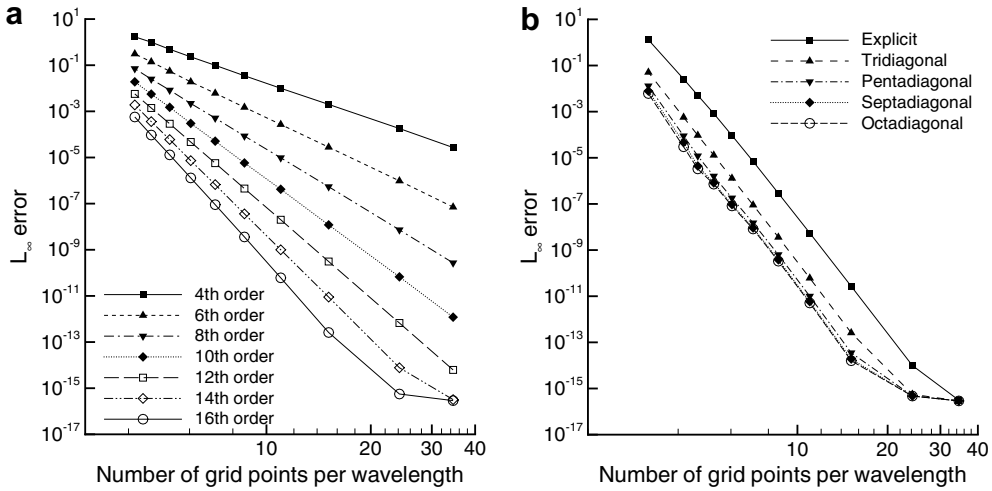


Fig. 3. $L_\infty$ errors for the solution of the wave equation using: (a) tridiagonal compact schemes for various orders of accuracy and (b) multi-diagonal compact schemes for 16th-order of accuracy, on a $49 \times 49$ grid.

Fig. 3(a) shows the maximum point wise error of the numerical solutions obtained using various high-order schemes for 10 runs with different values of $\omega$ against the number of grid points per wavelength, defined as $2\pi/(\omega h_{\max})$, where $h_{\max}$ represents the maximum grid spacing. As $\omega$ increases, the number of modes in the domain increase and there are less grid points to resolve each wave mode. The results clearly reveal the ability of higher order schemes to resolve the high wavenumber modes. When $\omega$ is small there are more grid points in resolving the wave modes and the magnitude of error remains small for various schemes. However as $\omega$ increases the number of grid points available to resolve the particular wave mode decrease and the advantage of using a higher order scheme is evident.

We further compare the resolution properties of multi-diagonal high-order compact schemes on a non-uniform grid for a fixed order of accuracy of 16. The multi-diagonal schemes are constructed by increasing the bandwidth of the matrix $P$ and decreasing the bandwidth of the matrix $Q$ in (8). Also note that the explicit scheme corresponds to a scheme with matrix $P$ equivalent to identity matrix. Fig. 3(b) shows the maximum point wise error of the numerical solutions obtained using various multi-diagonal high-order compact schemes for runs with different $\omega$. The results show that for small wavenumber $\omega$ all the schemes including the 16th-order explicit scheme give nearly same accuracy solutions. However as $\omega$ increases there are less grid points to resolve each wave mode and it is observed that the explicit scheme shows significant error when compared to the multi-diagonal schemes. For example at a wavenumber $\omega$ of 76/3, when the number of points per wavelength is close to 3, the octadiagonal gives the most accurate result with maximum point wise error of less than 0.1% whereas explicit scheme gives the least accurate result with the maximum point wise error exceeding 100%. It is noted that these results are consistent with previous studies [8] which show that the multi-diagonal schemes show smaller truncation error and have better resolution at higher wavenumbers than the corresponding explicit scheme for the same order of accuracy.

Next, we present a comparison of the computational cost involved in completing $10^5$ steps of time advancement for the solution of one-dimensional linear wave equation, and the accuracy of the numerical solution using various compact schemes on different non-uniform grids, in Fig. 4(a). Wavenumber $\omega$ for this set of computations is equal to 64/3. We observe that for the same computational expense, the high-order compact schemes offer a significant advantage in accuracy when compared to the lower order schemes. A similar comparison for the multi-diagonal schemes is shown in Fig. 4(b), for computations using $\omega = 76/3$. The better resolution ability of the multidiagonal high-order compact schemes, when compared to an explicit scheme of the same order of accuracy, is apparent.

The numerical tests on the linear wave equation confirm the accuracy and the stability of the high-order non-uniform grid compact schemes. It is also noted that the pentadiagonal and the multi-diagonal schemes, with a longer bandwidth of the matrix $P$, offer slightly better resolution than the tridiagonal compact schemes,

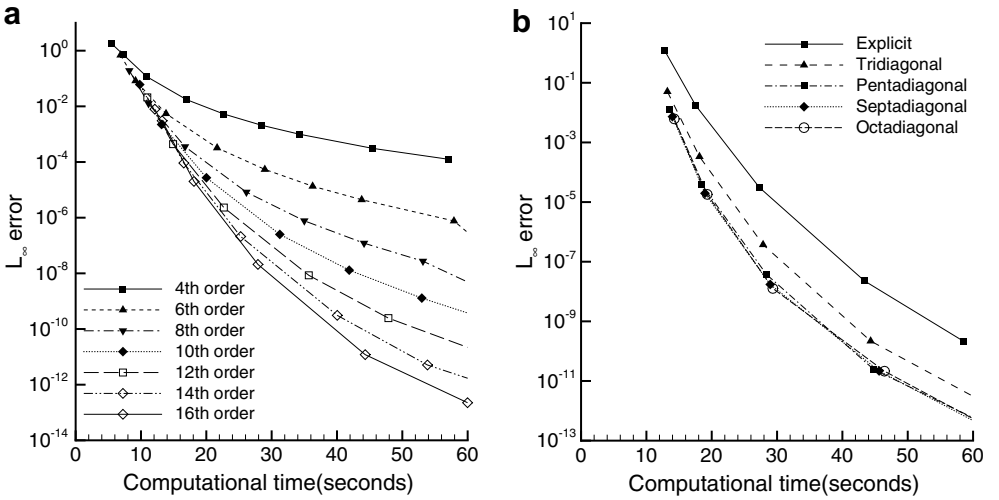


Fig. 4. Computational cost and accuracy obtained on integrating the one-dimensional wave equation using: (a) tridiagonal compact schemes for various orders of accuracy and (b) multi-diagonal compact schemes for 16th-order of accuracy.

for the same order of accuracy. However, explicit analytical expressions for the coefficients of a general compact scheme for the second derivative are available only for the tridiagonal schemes, and the calculation of these coefficients for other multidiagonal schemes requires numerical solution of a linear system [21]. For this reason only tridiagonal compact schemes are used in the present work for the solution of the incompressible Navier–Stokes equations and applications involving use of high-order compact schemes with longer bandwidth of the derivative stencil are left for future work.

### 5.2. Driven cavity flow with upper lid moving with variable velocity

In the following we apply the incompressible Navier–Stokes solver described in Section 4 to the solution of the driven cavity flow with the upper lid moving at a prescribed variable velocity $U_0(x)$ as shown in Fig. 1.

#### 5.2.1. Analytical driven cavity

In this test case, taken from [47,48], we consider flow in a square cavity with the upper lid moving with $U_0(x) = \zeta_1(x)\zeta_2'(1)$. The functions $\zeta_1(x)$ and $\zeta_2(y)$ are chosen to be polynomials which ensure that there is no discontinuity in not only the velocity but also the vorticity at the two upper corners of the square domain $\Omega = [0,1]^2$. The purpose here is to compare the numerical solution with the exact analytical solution and to examine the high-order of accuracy of compact schemes on non-uniform grids. In order to obtain an analytical solution, a vertical forcing term given by

$$f_y(x,y;Re) = \frac{1}{Re}[\zeta_2''''(y)\int \zeta_1(x)\,dx + 2\zeta_1'(x)\zeta_2''(y) + \zeta_1'''(x)\zeta_2(y)] + [\zeta_1^2(x)\{\zeta_2(y)\zeta_2'''(y) - \zeta_2'(y)\zeta_2''(y)\} - \zeta_2(y)\zeta_2'(y)\{\zeta_1(x)\zeta_1''(x) - \zeta_1'^2(x)\}], \tag{30}$$

is applied to the whole square domain, $\Omega = [0,1]^2$. The exact analytical solution is then given by [47,48]

$$u_e(x,y) = \zeta_1(x)\zeta_2'(y), \quad v_e(x,y) = -\zeta_1'(x)\zeta_2(y), \quad \omega_e(x,y) = -\{\zeta_1''(x)\zeta_2(y) + \zeta_1(x)\zeta_2''(y)\}. \tag{31}$$

Reynolds number $Re$ is set equal to 1000 along with $\zeta_1(x) = (x - x^2)^8$ and $\zeta_2(y) = 2^{10}(y^{16} - y^8)$ for this set of computations. Fig. 5(a) and (b) depict the streamlines and the iso-vorticity contours of the computed solution, respectively, obtained using a 16th-order compact scheme on a $49 \times 49$ ($\alpha = 0.95$) non-uniform grid; the computations on the corresponding uniform grid with $\alpha = 1$ are unstable. Fig. 6 shows the $L_\infty$ (maximum) norm of the error in the velocity and the vorticity fields defined as

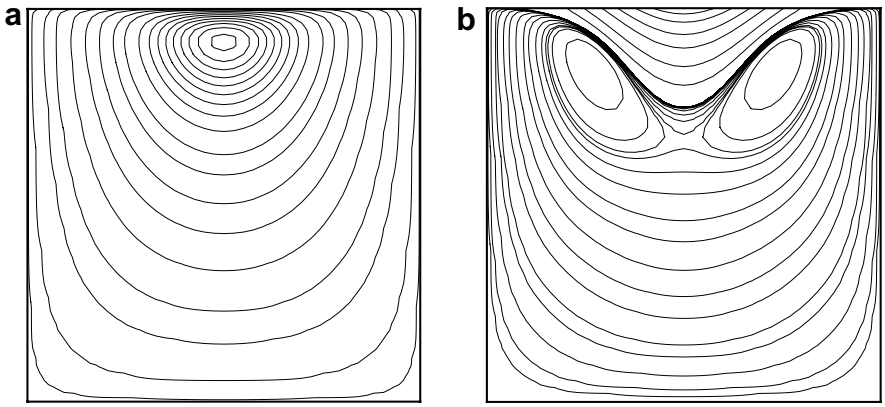


Fig. 5. (a) Streamlines and (b) iso-vorticity contours for the analytical driven cavity at $Re = 1000$ computed using a 16th-order compact scheme on a $49 \times 49$ non-uniform grid with $\alpha = 0.95$.

$$E_{\mathbf{U}} = \|u - u_{\mathrm{e}}\|_{\infty} + \|v - v_{\mathrm{e}}\|_{\infty} = \max_{1 \leqslant i,j \leqslant N} |u_{ij} - u_{\mathrm{e},ij}| + \max_{1 \leqslant i,j \leqslant N} |v_{ij} - v_{\mathrm{e},ij}|,$$
$$E_{\omega} = \|\omega - \omega_{\mathrm{e}}\|_{\infty} = \max_{1 \leqslant i,j \leqslant N} |\omega_{ij} - \omega_{\mathrm{e},ij}|, \tag{32}$$

for computations performed on $33 \times 33$ ($\alpha = 0.9$), $49 \times 49$ ($\alpha = 0.95$), $65 \times 65$ ($\alpha = 0.975$) and $97 \times 97$ ($\alpha = 0.99$) grids. It is observed that the error decreases with the increasing order of the compact schemes for the same computational grid. It may also be noted that since this problem is completely specified by 16th-order polynomials, a 16th-order non-uniform grid compact scheme yields solutions (not shown in the figure) with the maximum point wise error close to the numerical machine precision.

### 5.2.2. Singular driven cavity flow

The analytical driven cavity flow serves as a useful test problem for establishing the high-order of accuracy of the compact schemes on non-uniform grids. However, a more realistic and practical test problem is the singular driven cavity problem in which the upper lid moves with a constant unit horizontal velocity. We employ

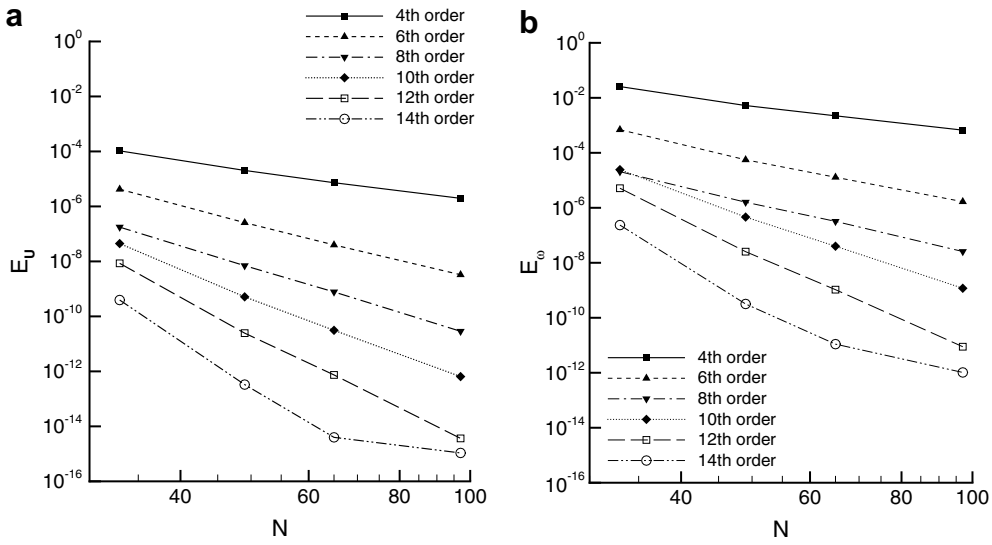


Fig. 6. Error in: (a) velocity and (b) vorticity fields for the high-order compact scheme solutions of the analytical driven cavity problem on various grid resolutions.

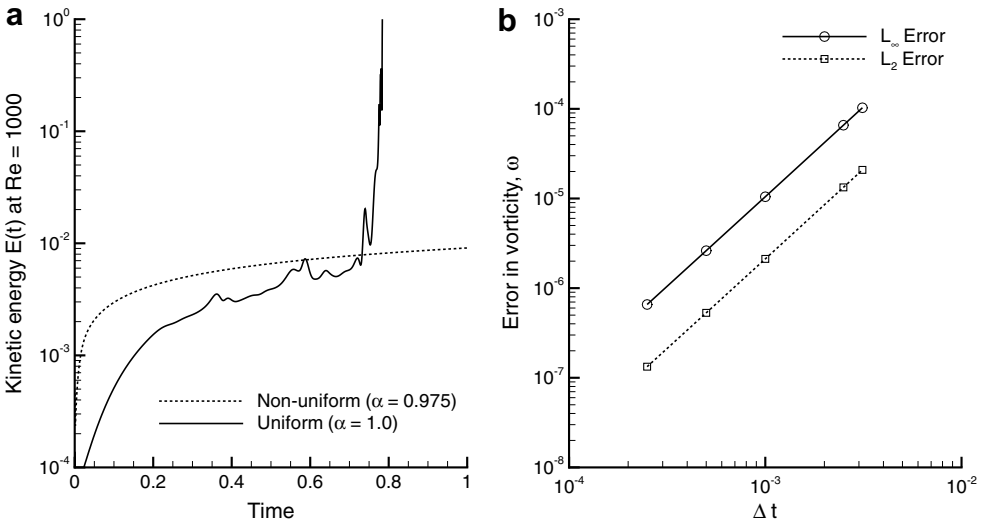


Fig. 7. (a) Kinetic energy vs. time for the solution of singular driven cavity flow at $Re = 1000$, computed using 12th-order compact scheme on a $65 \times 65$ grid. (b) Errors in vorticity at $t = 6.25$ for $Re = 1000$ computed on a $97 \times 97$ non-uniform grid with $\alpha = 0.99$ using a 16th-order compact scheme with various time step sizes.

the desingularization method described in Section 2.2 to obtain accurate solutions and to make a comparison with the previously published spectral benchmark solutions of Botella and Peyret [27].

Before making an assessment of the accuracy of the computed solutions we check for the numerical stability of the computations on uniform and non-uniform grids. Fig. 7(a) shows a plot of the evolution of the total kinetic energy of the driven cavity given by

$$E(t) = \frac{1}{2}\int_0^1 \int_0^1 \{u^2(x,y,t) + v^2(x,y,t)\}\,\mathrm{d}x\,\mathrm{d}y, \tag{33}$$

for computations with $Re$ equal to 1000 on $65 \times 65$ uniform and non-uniform grids. The time step-size $\Delta t$ is set equal to $10^{-2}$. To the best of our knowledge quadrature rules employing high-order compact schemes on non-uniform grids are not available and the method used in the current work in order to compute integrals, such as those arising in (33), is discussed in Appendix A. We observe that the computations on a uniform grid employing 12th-order compact finite difference scheme are unstable whereas those employing the same scheme on a non-uniform grid, with grid stretching parameter $\alpha = 0.975$, remain stable. All the high-order compact schemes on a non-uniform grid, with the same order of boundary closure as the interior, remain stable provided enough grid points are clustered at the boundary in accordance with the grid stretching parameter $\alpha$ listed in Table 2.

Next we study the temporal accuracy of the incompressible flow solver for the unsteady solutions. Following [33] solutions to the singular driven cavity flow are computed for $Re = 1000$ at a non-dimensional time $t = 6.25$. A 16th-order compact scheme on a $97 \times 97$ non-uniform grid with $\alpha = 0.99$ is utilized and runs are made for a range of values of time step size $\Delta t$. The solution obtained using a time step size of $\Delta t = 10^{-5}$ is taken as the reference exact solution and the error based on vorticity is calculated for various other time step sizes as

$$e_{i,j}(\Delta t) = \omega_{i,j}|_{\Delta t} - \omega_{i,j}|_{\Delta t = 10^{-5}}, \quad 0 \leqslant i \leqslant N_x, \;\; 0 \leqslant j \leqslant N_y. \tag{34}$$

Fig. 7(b) shows the $L_2$ and $L_\infty$ norms of the error $e$ as a function of time step size $\Delta t$. The second-order slope of the curve indicates that the employed AB/BDI-2 scheme is indeed $O((\Delta t)^2)$ accurate.

In order to evaluate the spatial accuracy of the high-order compact schemes in solving the singular driven cavity problem, we perform computations on non-uniform grids with $33 \times 33$, $49 \times 49$, $65 \times 65$, $97 \times 97$ and $151 \times 151$ grid points and $\alpha$ as prescribed in Table 2. Table 3 shows numerical comparison of the vorticity values along the horizontal ($y = \frac{1}{2}$) and the vertical ($x = \frac{1}{2}$) centerlines of the cavity computed using a 16th-order

Table 3
Convergence of vorticity $\omega$ through the horizontal and the vertical centerlines of the cavity for flow at $Re = 1000$ obtained using a 16th-order compact scheme

| | $x, y$ | $49 \times 49$ | $65 \times 65$ | $97 \times 97$ | $151 \times 151$ | Ref. [27] |
|---|---|---|---|---|---|---|
| $\omega(x,0.5)$ | 0.0000 | −5.46328 | −5.46197 | −5.46213 | −5.46216 | −5.46217 |
| | 0.0391 | −8.24642 | −8.24605 | −8.24614 | −8.24616 | −8.24616 |
| | 0.0547 | −6.50940 | −6.50868 | −6.50866 | −6.50867 | −6.50866 |
| | 0.1406 | 3.43030 | 3.43016 | 3.43016 | 3.43016 | 3.43016 |
| | 0.5000 | 2.06738 | 2.06722 | 2.06722 | 2.06722 | 2.06722 |
| | 0.7734 | 2.00283 | 2.00173 | 2.00174 | 2.00174 | 2.00174 |
| | 0.9062 | −0.82401 | −0.82402 | −0.82398 | −0.82398 | −0.82398 |
| | 0.9297 | −1.50176 | −1.50308 | −1.50306 | −1.50306 | −1.50306 |
| | 1.0000 | −7.66320 | −7.66374 | −7.66370 | −7.66369 | −7.66369 |
| $\omega(0.5, y)$ | 1.0000 | 14.3501 | 14.7427 | 14.7536 | 14.7534 | 14.7534 |
| | 0.9688 | 9.38136 | 9.45966 | 9.49498 | 9.49495 | 9.49496 |
| | 0.9531 | 4.64727 | 4.85454 | 4.85761 | 4.85754 | 4.85754 |
| | 0.7344 | 2.09130 | 2.09122 | 2.09121 | 2.09121 | 2.09121 |
| | 0.5000 | 2.06738 | 2.06722 | 2.06722 | 2.06722 | 2.06722 |
| | 0.2813 | 2.26788 | 2.26773 | 2.26772 | 2.26772 | 2.26772 |
| | 0.1016 | −1.63460 | −1.63439 | −1.63436 | −1.63436 | −1.63436 |
| | 0.0625 | −2.31805 | −2.31785 | −2.31786 | −2.31786 | −2.31786 |
| | 0.0000 | −4.16607 | −4.16639 | −4.16647 | −4.16648 | −4.16648 |

compact scheme on various grids. The benchmark spectral solutions of [27] obtained using $160 \times 160$ Chebyshev modes are also tabulated for comparison. It is observed that the solutions show a consistent convergence towards the benchmark results, with the solution on $151 \times 151$ grid showing differences in the vorticity values that are less than $10^{-5}$ in magnitude. Note that in all these tabulated cases we use the high-order compact polynomial interpolation [21] to obtain the values of flow variables at points that do not coincide with the grid nodes. The characteristic features of the flow computed on a $97 \times 97$ grid ($\alpha = 0.99$) using a 16th-order compact scheme are depicted in Fig. 8(a) and (b). The choice of streamlines and iso-vorticity lines values is the same as in [27] and we observe that the qualitative flow features of the problem are reproduced very accurately.

An estimation of error in terms of the relevant norms should give us an indication of the accuracy of the computed solutions. In absence of analytical solutions for the singular driven cavity an estimate on the error has to be obtained by using a high-order solution on a refined grid as the reference exact solution. However, since the problem is singular the global nature of compact schemes is expected to pollute the computed solution near the two top corners A and B. Note that Botella and Peyret [27] used a 10th-order filtering scheme in connection with spectral collocation method in order to obtain results with good convergence near the two singular corners. In order to avoid the singularity, in our present work we analyze the convergence of velocity field sufficiently far from the two corners and define errors in the horizontal velocity along the vertical centerline and the vertical velocity along the horizontal centerline as

$$\begin{aligned} E_u &= \|u(0.5, y) - u_e(0.5, y)\|_\infty = \max_{1 \leqslant j \leqslant N} |u_{(N_x-1)/2,j} - u_{e,(N_x-1)/2,j}| \\ E_v &= \|v(x, 0.5) - v_e(x, 0.5)\|_\infty = \max_{1 \leqslant i \leqslant N} |v_{i,(N_y-1)/2} - v_{e,i,(N_y-1)/2}|. \end{aligned} \tag{35}$$

The reference exact solution $u_e$, $v_e$ is obtained by interpolating the solution obtained using a 16th-order compact scheme on a $151 \times 151$ grid with $\alpha = 0.996$ to the nodes of the coarser grids. Fig. 8(c) and (d) show the errors $E_u$ and $E_v$ plotted against the number of grid points for various high-order compact schemes. A general trend of decreasing errors with increasing grid nodes for each of the high-order compact schemes is confirmed. However, we note that the errors do not necessarily decrease with increasing orders of accuracy. We believe that the reason for this is the presence of singularities in the driven cavity problem. Even though we solve a more regular problem obtained by singularity subtraction, only the first two terms in the series expansion of the singular solution are retained. We have also observed convergence of numerical

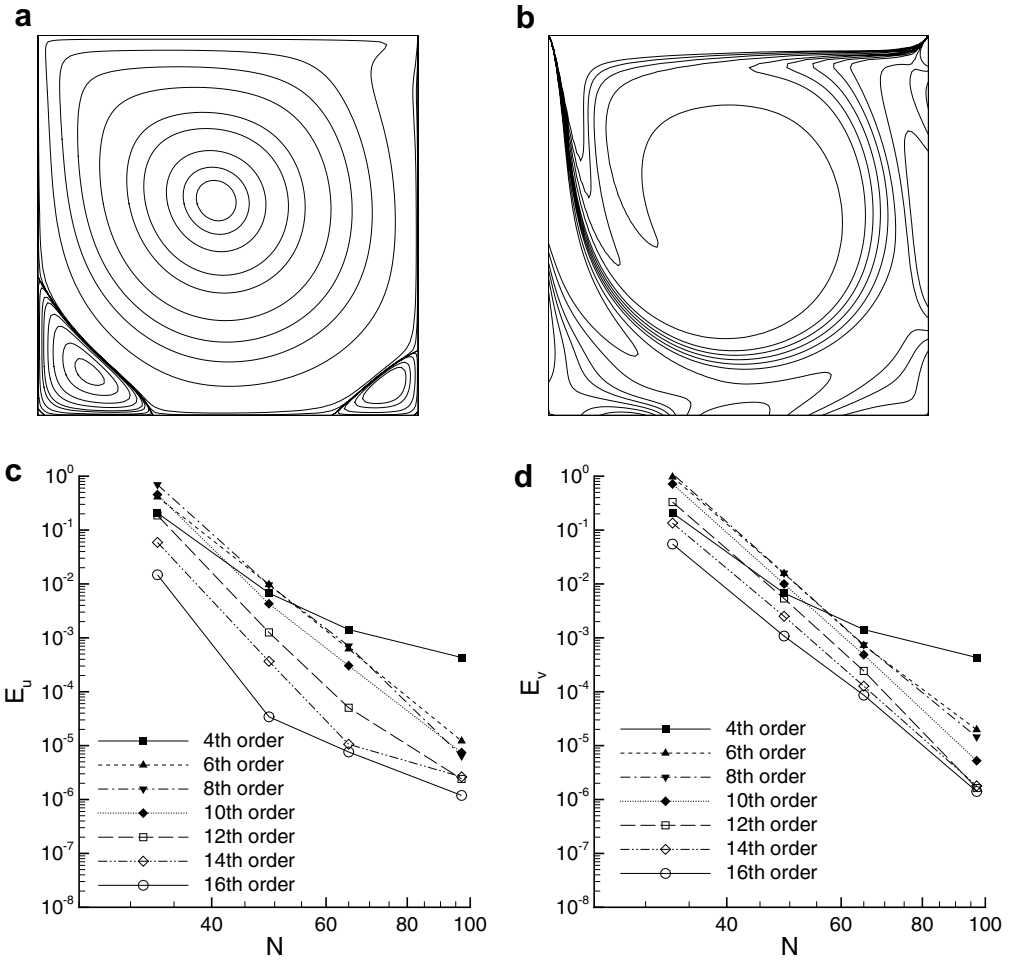


Fig. 8. (a) Streamlines and (b) iso-vorticity contours for $Re = 1000$ computed using 16th-order compact scheme on $97 \times 97$ non-uniform grid with $\alpha = 0.99$. Errors (c) $E_u$ and (d) $E_v$ for various grid resolutions using different high-order compact schemes for flow at $Re = 1000$.

solutions to be even worse (results are not presented here) when only the first Stokes term is retained in the analytical solution for the purpose of computations and hence more singular terms need to be retained in order to obtain better convergence. In spite of this behavior we note that the magnitude of error for the high-order schemes remains quite small with a 16th-order scheme on a $65 \times 65$ grid giving maximum point-wise errors of less than $10^{-4}$.

A further illustration of the accuracy and the efficiency of the non-uniform grid compact schemes is given by computation of the unsteady flow at higher $Re$ of 9000 and 10,000. Previous work by Auteri et al. [33] has established that the singular driven cavity flow shows Hopf bifurcation from steady flow to unsteady periodic flow at a critical $Re$ which lies in the interval $8017.6 \leqslant Re_c \leqslant 8018.8$. Thus for the computations at $Re = 9000$ and 10,000 we expect the flow to show unsteady periodic behavior which needs the use of accurate long time integration of the governing equations. For these cases we perform computations on a $151 \times 151$ grid using a 20th-order compact scheme on a non-uniform grid with $\alpha = 0.993$ according to Table 2. Computations are done for nearly two million time-steps with $\Delta t = 10^{-3}$ starting from the steady-state solution at $Re = 1000$. The choice of the time step size $\Delta t$ is sufficiently small when compared to the smallest Kolmogorov time scale, $\tau = \sqrt{\nu L/U^3} = 10^{-2}$ for the flow at $Re = 10^4$. This ensures that the smallest temporal scales of the flow are resolved accurately. Following previous studies the criterion used for monitoring the time evolution of the flow is chosen to be the kinetic energy $E(t)$, defined by (33).

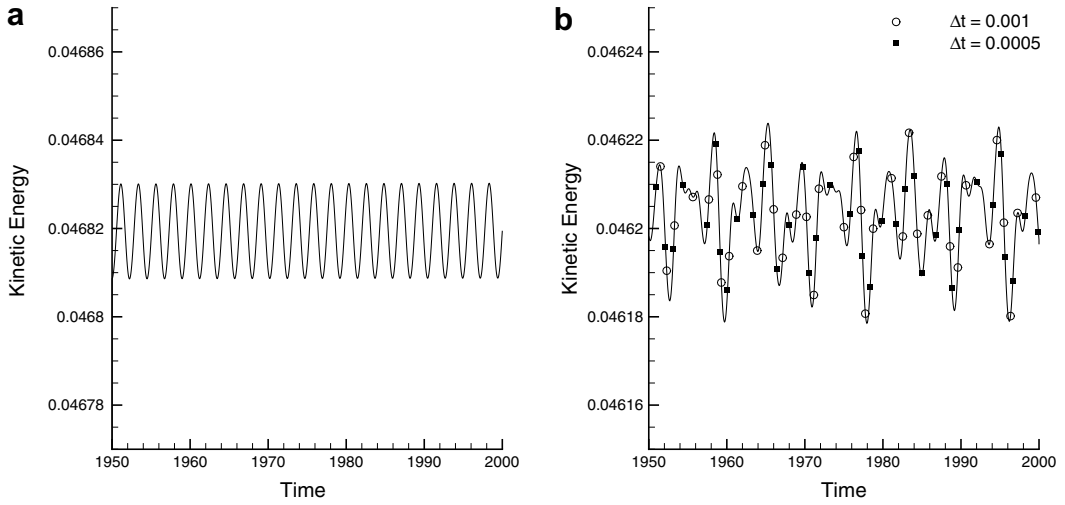


Fig. 9. Kinetic energy as a function of time for the flow at $Re$ equal to: (a) 9000 and (b) 10,000.

Fig. 9(a) and (b) depict the kinetic energy of the singular driven cavity as a function of time for flow at $Re$ equal to 9000 and 10,000. Sizeable fluctuations are observed in the kinetic energy for flow at $Re = 9000$ and 10,000. For the flow at $Re = 9000$ we compute the maxima and the minima in the horizontal and the vertical velocities at the center of the cavity $(0.5, 0.5)$ as

$$u_{\max} = 0.02753(0.02752)^*, \quad u_{\min} = 0.02712(0.02711)^*, \quad v_{\max} = 0.00938(0.00942)^*, \quad v_{\min} = 0.00898(0.00901)^*. \tag{36}$$

The period of the extrema of the kinetic energy is, in our case, $2.247 \pm 10^{-3}$ $(2.2456 \pm 8 \times 10^{-4})^*$[1]; these values match extremely well with the results of Botella and Peyret [28] who used a Chebyshev collocation method.

Next we compare the qualitative features of the unsteady flow at $Re = 10{,}000$. The variation of the kinetic energy for the flow at $Re = 10{,}000$ as shown in Fig. 9(b) is found to be consistent with the results in [36]. Slight difference between the actual values of kinetic energy is attributed to the fact that an exponential ramp profile was employed in the simulations in [36] to smoothen the discontinuity in the horizontal velocity at the two upper corners. Another set of calculations for the unsteady flow at $Re = 10{,}000$ is performed using the same grid but a reduced time step of $\Delta t = 5 \times 10^{-4}$. The result of the variation of the kinetic energy with time is shown in Fig. 9(b) against the results obtained using $\Delta t = 10^{-3}$. The two results are found to be extremely close to each other and thus certify the accuracy of the unsteady flow computations at high $Re$. The smooth streamlines and iso-vorticity contours for the quasiperiodic unsteady flow at $Re = 10{,}000$ at three different time instants are shown in Fig. 10.

In order to assess the resolution capabilities of various high-order schemes we next present some numerical results computed for the singular driven cavity flow at $Re = 7500$ using various high-order compact schemes on the same $151 \times 151 (\alpha = 0.996)$ grid. Fig. 11 shows the iso-vorticity contours obtained using 4th, 10th and 16th-order compact schemes, respectively. We observe that the solutions employing the lowest order scheme (4th-order) show oscillations with wavelengths of grid spacing in the iso-vorticity contours, close to the upper moving wall. For a 10th-order scheme the contours are resolved better than the 4th-order scheme, but some oscillations are still present. For a still higher order of 16, as depicted in Fig. 11, the iso-vorticity contours are fully resolved and the computed solution is free of oscillations. Thus the iso-vorticity contours are better resolved through the use of higher order compact schemes for a given fixed grid. Note that the computed solution is smooth in most of the remaining domain. The reason for this is that there are sharp gradients close to the upper moving wall and hence for this choice of computational grid $(151 \times 151)$ high-resolution (order)

[1] quantities in $()^*$ are from [28].

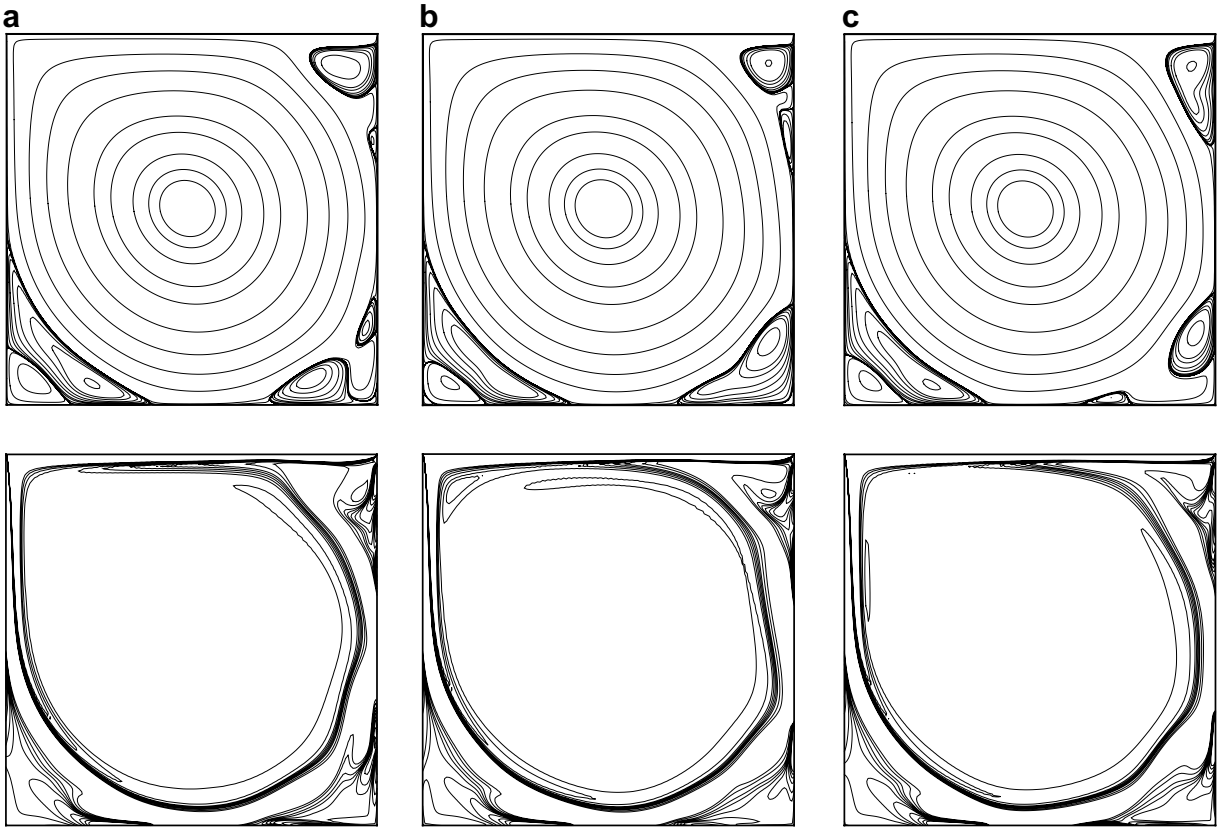


Fig. 10. Streamlines (top) and iso-vorticity (bottom) contours for the flow at $Re = 10{,}000$ computed at times $t =$ (a) 2003.5; (b) 2008.75; (c) 2014.0.

schemes are required to capture these flow features accurately. Alternatively, a refined grid could also be employed without increasing the order of the scheme. The streamfunction is much more regular and smooth streamlines are computed for all the higher-order compact schemes (results are not shown here).

Thus the driven cavity flow results show that the high-order non-uniform grid compact schemes are stable for very high-orders (tested up to 20th-order) of accuracy and provide increased resolution, which is essential for high $Re$ computations. Such high-order solutions are not possible using a conventional uniform grid compact scheme due to numerical instability.

### 5.3. Natural convection in a differentially heated square cavity

In this section we perform computations for natural convection of air (Prandtl number = 0.71) in a square cavity whose top and bottom walls are adiabatic and lateral walls are maintained at different temperatures. Benchmark solutions to this problem obtained using a 2nd-order finite difference scheme and a Chebyshev collocation spectral method are documented in [45,46], respectively. Note that this problem is free of any singularity in the boundary conditions, except the presence of corners and hence is more attractive for testing high-order compact schemes. The governing equations for this problem are the incompressible Navier–Stokes equations for the unsteady two-dimensional flows in terms of variables vorticity $\omega$ and stream function $\psi$, which are supplemented by the energy equation for the non-dimensional temperature $\theta$:

$$\frac{\partial \omega}{\partial t} + J(\omega,\psi) = \frac{Pr}{\sqrt{Ra}}\nabla^2\omega + Pr\frac{\partial \theta}{\partial x}, \quad \frac{\partial \theta}{\partial t} + J(\theta,\psi) = \frac{1}{\sqrt{Ra}}\nabla^2\theta, \quad \nabla^2\psi = -\omega, \tag{37}$$

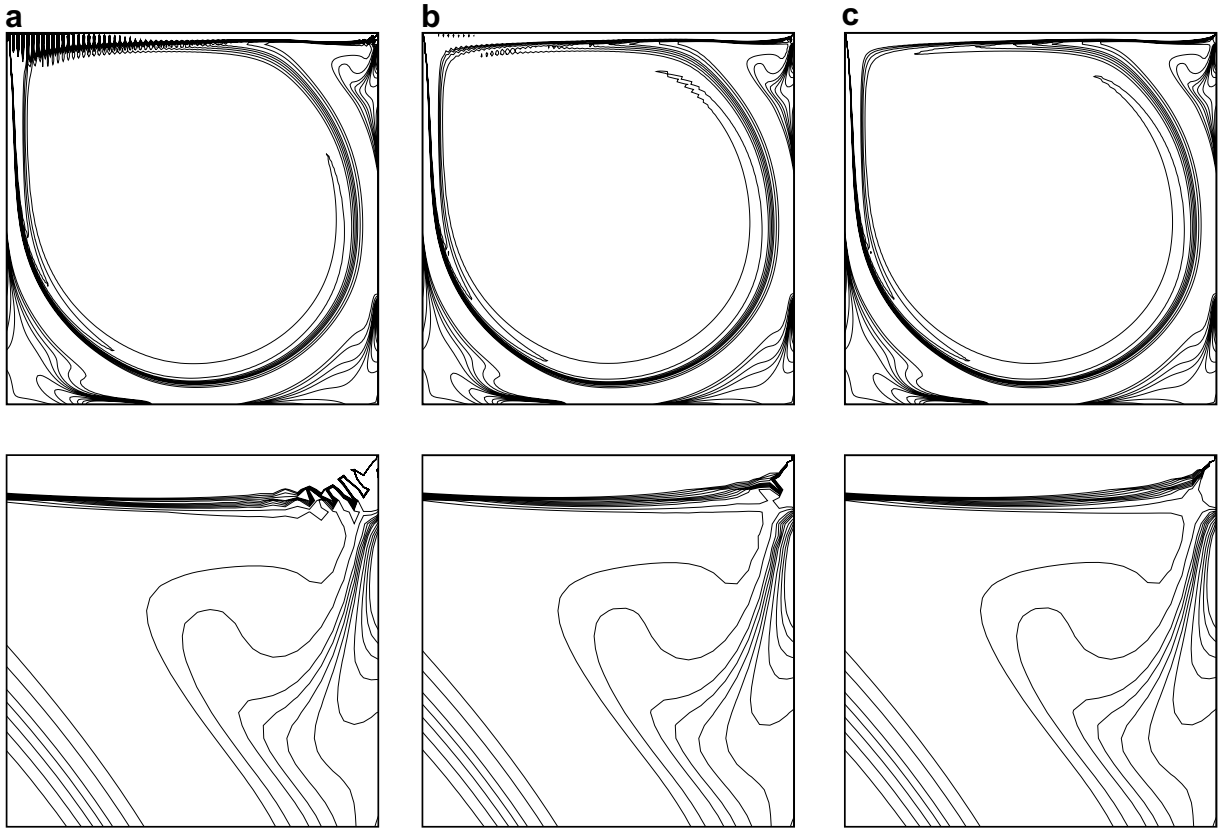


Fig. 11. (Top) Iso-vorticity contours and (bottom) close up of the contours in the upper right corner, for the flow at $Re = 7500$ obtained using: (a) 4th; (b) 10th and (c) 16th-order schemes.

where $Pr$ is the Prandtl number and $Ra$ denotes the Rayleigh number. The boundary conditions for $\psi$ and $\theta$ are given by

$$\psi|_{\partial\Omega} = \left.\frac{\partial\psi}{\partial x}\right|_{x=0,1} = \left.\frac{\partial\psi}{\partial y}\right|_{y=0,1} = 0, \quad \text{and} \quad \theta(0,y) = 0.5, \quad \theta(1,y) = -0.5, \quad \left.\frac{\partial\theta}{\partial y}\right|_{y=0,1} = 0. \tag{38}$$

Discretization of these equations following a procedure similar to the one for the driven cavity flow leads to following discrete algebraic equations

$$\begin{aligned} &(\nabla_{\mathrm{d}}^2 - \overline{\gamma})\theta^{n+1} = S_{\theta}^{n,n-1}, \\ &\left(\nabla_{\mathrm{d}}^2 - \frac{\overline{\gamma}}{Pr}\right)\omega^{n+1} = S_{\omega}^{n,n-1}, \\ &\nabla_{\mathrm{d}}^2\psi^{n+1} = -\omega^{n+1}, \end{aligned} \tag{39}$$

subject to boundary conditions

$$\begin{aligned} &\psi^n = D_n\psi^n = 0 \quad \text{on } \partial\Omega_N, \\ &\theta^n|_{x=0,1} = 0.5, -0.5, \quad \text{and} \quad D_n\theta^n|_{y=0,1} = 0. \end{aligned} \tag{40}$$

These discrete algebraic equations are solved using an influence matrix technique which is very similar to the one employed for the driven cavity problem.

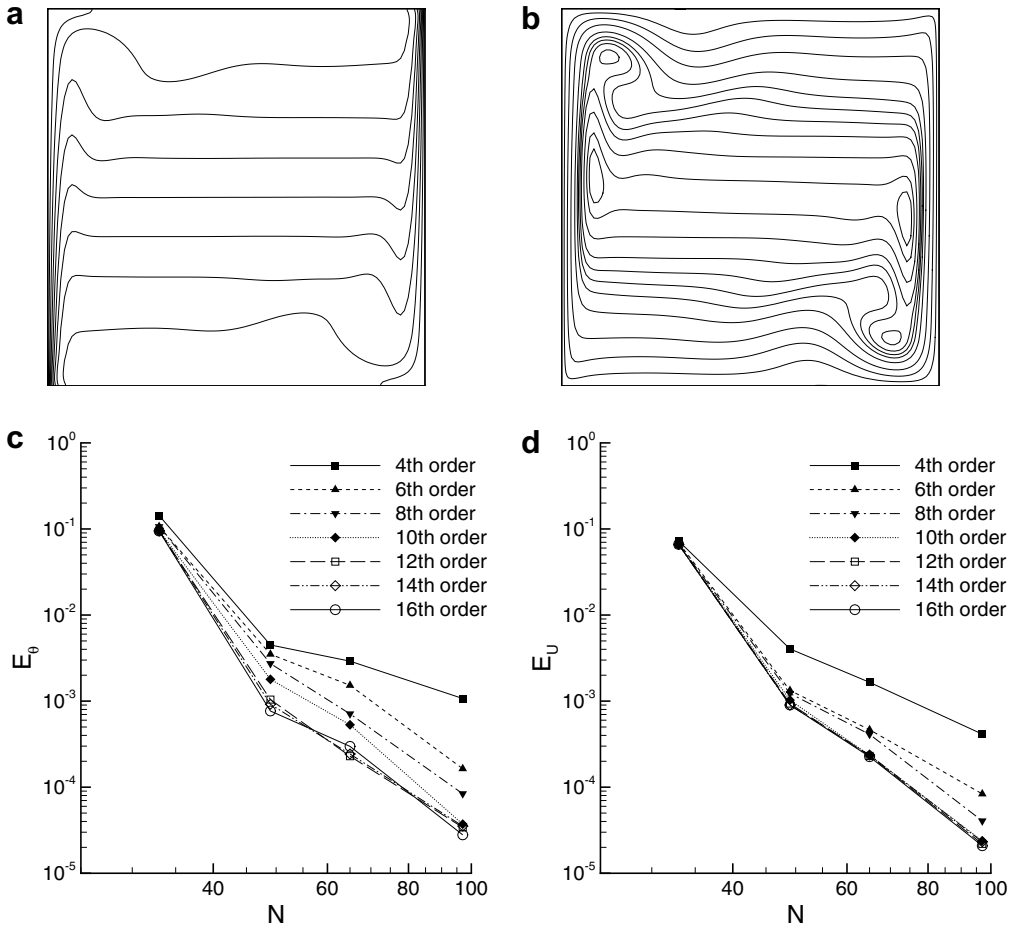


Fig. 12. (a) Isotherms and (b) streamlines for flow at $Ra = 10^7$ ($97 \times 97$ grid). Contour levels are same as in [46]. Errors in (c) temperature and (d) velocity field for various high-order compact schemes on different grid resolutions.

In order to evaluate the spatial accuracy of the high-order compact schemes in solving the natural convection problem we perform computations for $Ra = 10^7$, on non-uniform grids with $33 \times 33$, $49 \times 49$, $65 \times 65$, $97 \times 97$ and $151 \times 151$ grid points, and $\alpha$ as specified in the first row of Table 2 for orders of accuracy ranging from 4 to 16. Fig. 12(a) and (b) show the smooth isotherms and streamlines for the flow computed using a 16th-order compact scheme on a $97 \times 97$ non-uniform grid, respectively. In order to get a quantitative assessment on the accuracy of the high-order non-uniform grid compact schemes, we compute the error in the temperature and the velocity fields by treating the solution obtained by using the highest order scheme (16th) on the highest resolution grid ($151 \times 151$) as the exact solution. Fig. 12(c) and (d) show the maximum point-wise errors in the temperature and the velocity fields, $E_\theta$ and $E_U$ ($E_U$ given by the first equation in (32)), plotted against the number of grid points for various high-order compact schemes. It is noted that even though the error in the velocity and the temperature fields decreases when the order of accuracy of the schemes is increased from four to six, subsequent increases in order do not produce a significant decrease in error. In order to ensure that our error estimate is not affected by the grid resolution of the exact solution, we recompute the error based on an exact solution obtained from a 16th-order compact scheme on a refined $301 \times 301$ non-uniform grid, with the grid stretching parameter $\alpha$ as prescribed in Table 2. No discernible differences are observed from the error estimate shown in Fig. 12(c) and (d) (results are not shown here). We believe that the reason for these slow convergence rates of the very high-order schemes is the lack of sufficient regularity in the solution which is evident from the small scale features present in the flow field. As a result, the actual accuracy

achieved by the high-order compact schemes is limited by the resolution of the grid employed and not by their formal order. The Nusselt numbers along the vertical centerline $x = 0.5$, $Nu_{\frac{1}{2}}$, and the wall $x = 0$, $Nu_0$, defined as

$$Nu_{0,\frac{1}{2}} = \int_0^1 \left( \sqrt{Ra} u\theta - \frac{\partial \theta}{\partial x} \right)\Bigg|_{x=0,0.5} \mathrm{d}y, \tag{41}$$

computed using a 16th-order compact scheme on a $151 \times 151$ grid, in our case are 16.523; these are in perfect agreement with the benchmark results of [46] obtained using a spectral Chebyshev collocation method.

### 5.4. Viscous flow past a circular cylinder

As a final test of the accuracy of the high-order compact schemes we compute the solution for steady and unsteady flow past a two-dimensional circular cylinder. Due to its practical importance this problem has been extensively studied both experimentally [58,59] and through computations [49–57].

We consider a circular cylinder of unit radius, $R = 1$, which is placed in an infinite domain. Flow in the far-field is assumed to be given by the potential solution corresponding to a circular cylinder placed in a uniform flow with unit free stream velocity, $U_\infty = 1$. The geometry of the problem along with the computational grid employed to obtain the solution is shown in Fig. 13. The inner radius of the computational domain $r_{\min}$ is set equal to 1, corresponding to the radius of the cylinder. We consider the incompressible Navier–Stokes equations in polar $(r, \phi)$ vorticity–streamfunction formulation

$$\begin{aligned} &\frac{\partial \omega}{\partial t} + \frac{1}{r}\left( \frac{\partial \psi}{\partial \phi}\frac{\partial \omega}{\partial r} - \frac{\partial \psi}{\partial r}\frac{\partial \omega}{\partial \phi} \right) = \frac{1}{Re}\left\{ \frac{1}{r}\frac{\partial}{\partial r}\left( r\frac{\partial \omega}{\partial r} \right) + \frac{1}{r^2}\frac{\partial^2 \omega}{\partial \phi^2} \right\} \\ &\left\{ \frac{1}{r}\frac{\partial}{\partial r}\left( r\frac{\partial \psi}{\partial r} \right) + \frac{1}{r^2}\frac{\partial^2 \psi}{\partial \phi^2} \right\} = -\omega \end{aligned} \tag{42}$$

subject to the boundary conditions

$$\begin{aligned} &\psi(r_{\min}, \phi) = 0, \quad \psi(r_{\max}, \phi) = \left( r_{\max} - \frac{r_{\min}^2}{r_{\max}} \right) \sin\phi, \quad 0 \leqslant \phi \leqslant 2\pi, \\ &\left.\frac{\partial \psi}{\partial r}\right|_{r=r_{\min}} = 0, \quad \left.\frac{\partial \psi}{\partial r}\right|_{r=r_{\max}} = \left( 1 + \frac{r_{\min}^2}{r_{\max}^2} \right) \sin\phi, \quad 0 \leqslant \phi \leqslant 2\pi. \end{aligned} \tag{43}$$

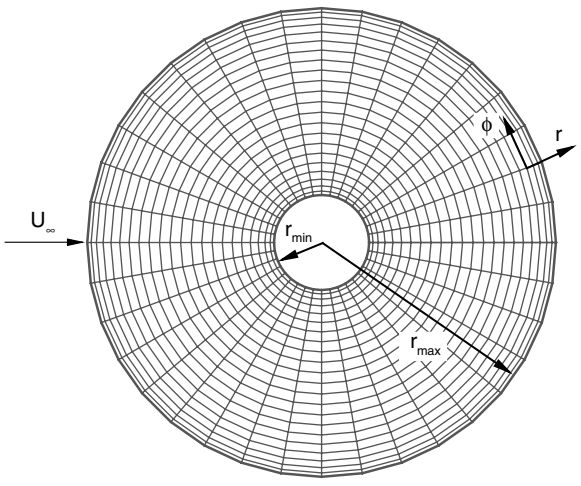


Fig. 13. Computational domain and a representative grid for the flow past a circular cylinder.

The Reynolds number $Re$ is based on the cylinder diameter and the remaining flow quantities: $\omega$, $\psi$ and time $t$ are non-dimensionalized based on the cylinder radius $R$, and $U_\infty$. The time discretization of (42) is accomplished through the AB/BDI-2 scheme. As shown in Fig. 13 we employ a computational grid which is uniform in the $\phi$ direction and non-uniform (stretched) in the radial direction:

$$\begin{aligned} r_i &= \frac{r_{\max}+r_{\min}}{2} + \left(\frac{r_{\max}-r_{\min}}{2}\right)\frac{\sin^{-1}(-\alpha\cos(\pi i/N_{\mathrm{r}}))}{\sin^{-1}\alpha}, \quad i = 0,\ldots,N_{\mathrm{r}} \\ \phi_j &= \frac{2\pi j}{N_\phi}, \quad j = 0,\ldots,N_\phi - 1. \end{aligned} \tag{44}$$

Since the problem is periodic in the azimuthal direction $\phi$ we use periodic higher order compact schemes on uniform grid for discretization along $\phi$. The discretization in the radial direction is achieved through the use of higher order compact schemes on the computational grid given by the first equation in (44) with the same order of boundary closures as the interior. We present computational results employing compact schemes with even orders of accuracy ranging from 4 to 20. In each of the test cases the order of uniform grid periodic and non-uniform grid compact schemes, utilized for discretization in $r$ and $\phi$ directions, respectively, is kept the same. The parameter $\alpha$ for discretization in the radial direction is chosen according to the values listed in the second row of Table 2 for the stability of the 20th-order non-uniform grid compact scheme. The resulting Poisson and Helmholtz equations are solved using matrix diagonalization method which is very similar to the one used in Cartesian coordinates. The values of vorticity at the outer and inner boundaries at $r_{\max}$ and $r_{\min}$ are determined using the influence matrix technique. The implementation of the algorithm is very similar to the one for the driven cavity, the only difference being the reduced size of the influence matrix ($2N_{\mathrm{r}} \times 2N_{\mathrm{r}}$) and its non-singularity which obviates the need for any special treatment (such as the removal of four boundary points in the case of a square domain).

*5.4.1. Transient flow past an impulsively started cylinder*

We start by presenting numerical results for the initial transient flow past an impulsively started cylinder. High accuracy solutions to this problem have been computed for a range of $Re$ using vortex methods [49,51] and 2nd and 4th-order finite difference method [50]. For these computations we set $r_{\max} = 16.0$ corresponding to the outer boundary of the computational domain. Time step size $\Delta t$ is chosen as $5 \times 10^{-4}$. We solve the problem on three grid resolutions, $301 \times 300$, $401 \times 400$ and $501 \times 501$ with $Re = 1000$. The transient solution is computed up to a non-dimensional time of 10.0.

Fig. 14 depicts the streamlines and iso-vorticity contours for the flow at a non-dimensional time of 6.0, computed using the 20th-order compact scheme on a $401 \times 400$ grid. We observe that the sharp gradients in vorticity and the small recirculating flow regions in the streamline contours are captured quite effectively by the 20th-order scheme. In Fig. 15(a) we show a comparison of the vorticity at the cylinder surface with

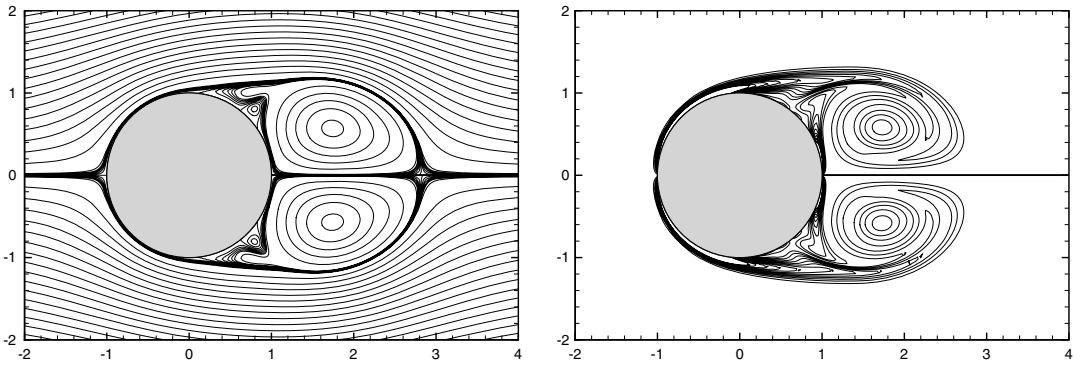


Fig. 14. Streamlines (left) and iso-vorticity (right) contours for flow at $Re = 1000$ obtained using 20th-order compact scheme on a $401 \times 400$ grid at time $t = 6.0$. Contour levels for the streamlines are $-4{:}0.1{:}4$, $-0.01{:}0.0025{:}0.01$ and $\pm 0.015$. Contour levels for the vorticity are $-12{:}1{:}12$.

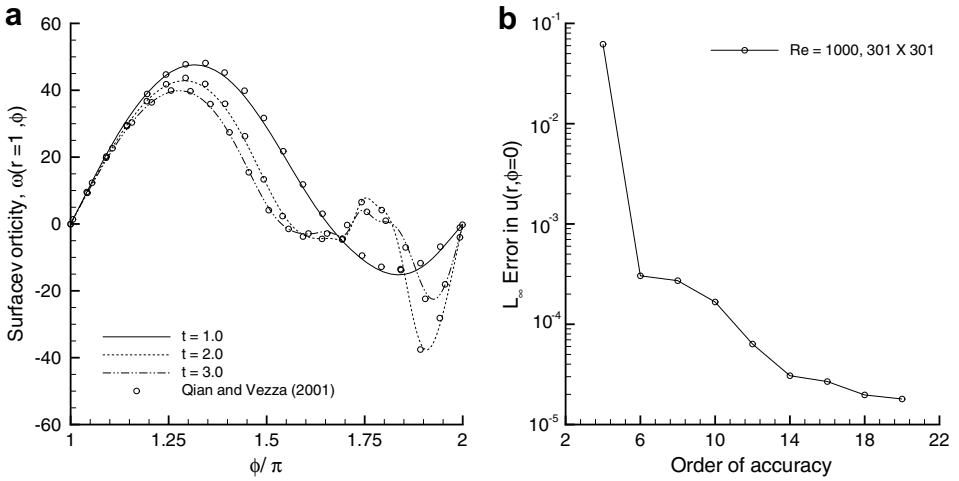


Fig. 15. (a) Vorticity on the surface of the cylinder at various times for $Re = 1000$. (b) Maximum point wise error in the radial velocity along the rear symmetry axis for various high-order compact schemes.

the results of [52] at various time instants. The agreement is satisfactory and establishes the high accuracy of both non-uniform grid compact schemes and uniform grid (periodic) compact schemes. In order to obtain a quantitative assessment on the accuracy we compute the maximum point wise error in radial velocity along the rear symmetry axis of the cylinder ($\phi = 0$), given by $u = (1/r)(\partial\psi/\partial\phi)$, at time $t = 6.0$ for various high-order compact schemes on $301 \times 300$ grid. The numerical solution obtained from the 20th-order scheme on $501 \times 500$ grid is treated as the exact solution. A plot of the error against the order of accuracy of the schemes employed is depicted in Fig. 15(b). We observe that the error continues to decrease with increasing order of accuracy with the maximum drop observed by increasing the order of accuracy from 4 to 6. At relatively higher orders of accuracy we no longer observe a decrease in error by increasing the order of the scheme. The most likely reason for this is the lack of regularity in the solution which is evident from the presence of small scale features in the flow field, and hence, the grid resolution and not the formal order, dictates the accuracy of the computed solutions.

*5.4.2. Long time computations for steady and unsteady flow*

In this section we demonstrate the stability and accuracy of the high-order compact schemes in long time integration of the incompressible Navier–Stokes equations for steady and unsteady flow over a circular cylinder. In order to minimize the effect of potential flow boundary conditions at the outer boundary we set $r_{\max} = 25.0$ for $Re = 20$ and 40 and $r_{\max} = 50.0$ for $Re = 100$. For the flow at $Re = 20$ and 40 we compute the final steady state solution and compare various parameters: the length of the wake bubble, the separation angle and the drag coefficient with previous studies. For the flow at $Re = 100$ various experimental and computational studies have predicted the well-known phenomena of periodic vortex shedding and for this case we compare the unsteady drag and lift coefficients and the Strouhal number. The drag and lift coefficients are computed using following formulas [49]

$$\begin{aligned} C_{\mathrm{D}} &= \frac{1}{Re}\int_0^{2\pi}\left(\frac{\partial\omega}{\partial r} - \omega\right)\Big|_{r=r_{\min}} \sin\phi\,\mathrm{d}\phi, \\ C_{\mathrm{L}} &= \frac{1}{Re}\int_0^{2\pi}\left(\frac{\partial\omega}{\partial r} - \omega\right)\Big|_{r=r_{\min}} \cos\phi\,\mathrm{d}\phi, \end{aligned} \tag{45}$$

where a cylinder radius of unity has been assumed for our present computations. The integral over $\phi$ along the cylinder surface is computed numerically using the trapezoidal rule which is quite accurate for a periodic domain [3].

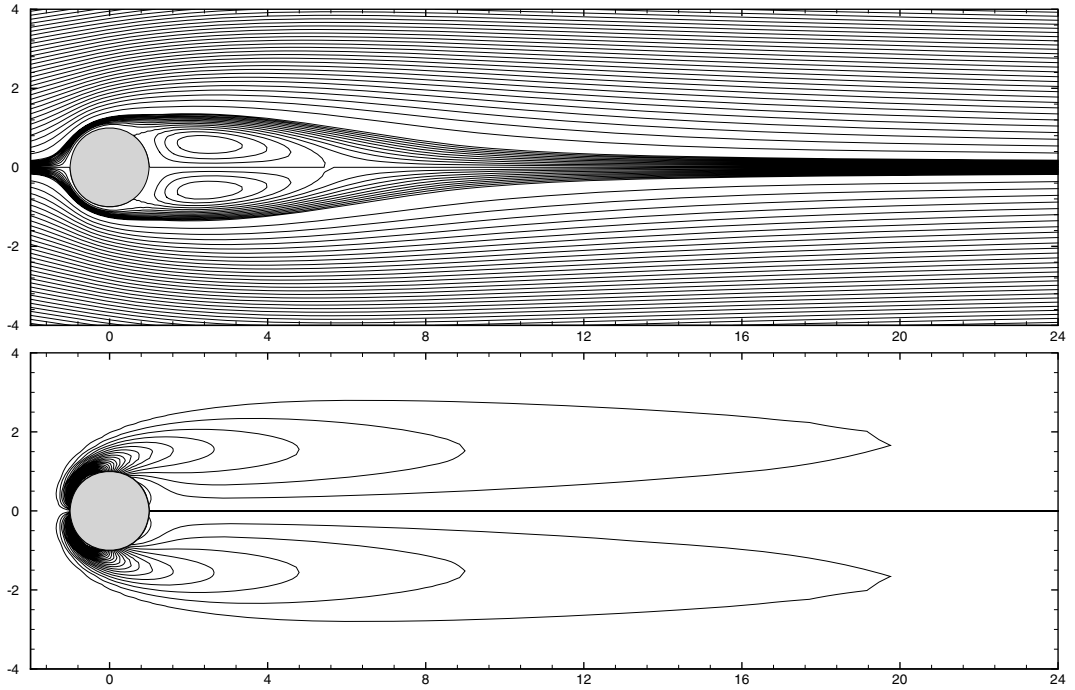


Fig. 16. Streamlines (top) and iso-vorticity (bottom) contours for flow at $Re = 40$ obtained using 20th-order scheme on a $201 \times 300$ grid. Contour levels for streamlines are $-10{:}0.1{:}10$, $-0.1{:}0.01{:}0.1$. Contour levels for the vorticity are $-5{:}0.2{:}5$.

We perform simulations for flows at $Re = 20$ and 40 employing $97 \times 150$, $151 \times 200$, $201 \times 300$, and $151 \times 200$, $201 \times 300$, grid resolutions, respectively. Non-dimensional time step size $\Delta t$ is chosen as 0.005 and the flow is computed up to a non-dimensional time of 1000.0 using various high-order compact schemes starting from the potential flow over the entire domain. Fig. 16 shows the streamlines and the iso-vorticity contours for the steady state flow at $Re = 40$. The contours agree well with those presented in [57].

A comparison of the values of the wake bubble length, angle of separation and coefficient of drag ($C_D$), computed in the present study by using a 20th-order compact scheme on a $201 \times 300$ grid resolution, with the previous studies is presented in Table 4. Good agreement is observed, in general, for both $Re = 20$ and 40. Next, we present results on convergence study for $C_D$ using various high-order compact schemes by treating the solution obtained on the finest grid ($201 \times 300$) as the exact one. Fig. 17(a) and (b) show the errors in $C_D$ for numerical solutions at $Re = 20$ and 40, respectively, plotted against the order of accuracy of the employed schemes. Note that the calculation of drag involves derivative of vorticity: a quantity which is more irregular than vorticity itself. Hence, we expect the effect of increasing orders of accuracy to be more pronounced in the computation of drag. This observation is verified from

Table 4
Wake bubble length ($L$), angle of separation ($\theta$), and drag coefficient for $Re = 20$ and 40

| | $Re = 20$ | | | $Re = 40$ | | |
|---|---|---|---|---|---|---|
| | $L$ | $\theta$ (°) | $C_D$ | $L$ | $\theta$ (°) | $C_D$ |
| Tritton [58] | – | – | 2.22 | – | – | 1.48 |
| Coutanceau and Bouard [59] | 0.73 | 42.3 | – | 1.89 | 52.8 | – |
| Fornberg [57] | 0.91 | – | 2.00 | 2.24 | – | 1.50 |
| Dennis and Chang [56] | 0.94 | 43.7 | 2.05 | 2.35 | 53.8 | 1.52 |
| Calhoun [54] | 0.91 | 45.5 | 2.19 | 2.18 | 54.2 | 1.62 |
| Linnick and Fasel [55] | 0.93 | 43.5 | 2.06 | 2.28 | 53.6 | 1.54 |
| Present | 0.92 | 43.2 | 2.07 | 2.34 | 52.7 | 1.55 |

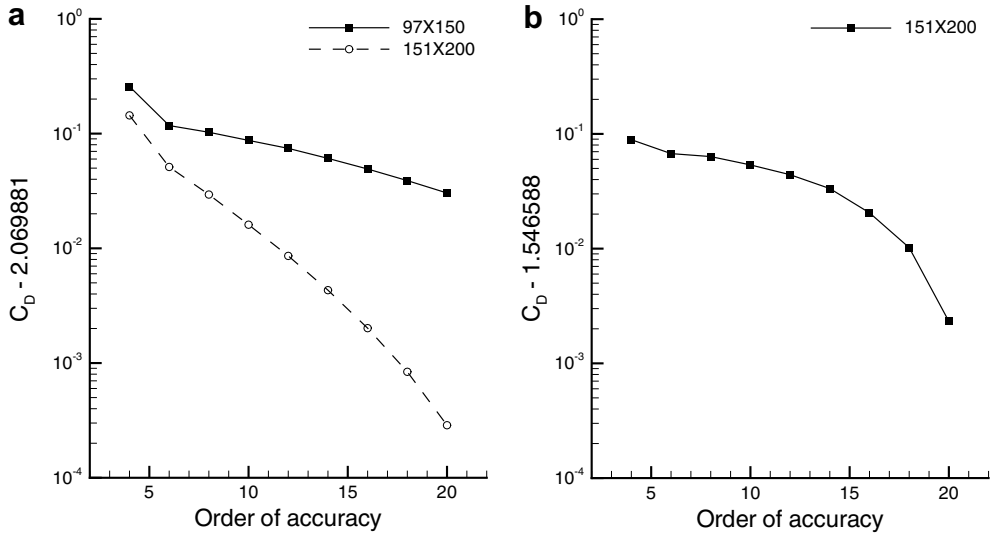


Fig. 17. Error in the drag coefficient against the order of accuracy for: (a) $Re = 20$ and (b) $Re = 40$. The numerals appearing on the ordinate axis represent values of drag computed on the finest grid.

Fig. 17(a) and (b), where the error in the computed value of drag coefficient continues to decay with increasing order of accuracy of the employed scheme and the 20th-order scheme gives most accurate value on coarser grids.

We now proceed to the numerical results for flow over a cylinder at $Re = 100$. Computations are performed on a $251 \times 300$ grid up to a non-dimensional time of 1000.0 using $\Delta t = 2.5 \times 10^{-3}$. As the time progresses flow shows an unsteady periodic behavior in the numerical solution. Fig. 18(a) and (b) show the periodic time dependent variation of the drag and lift coefficient for this flow. The value of the Strouhal number calculated from the variation of the lift coefficient is 0.1647 which shows excellent agreement with the previous study of Liu et al. [53] who reported a value of 0.165. The smooth iso-vorticity contours at two different time instants differing by 6.0 are shown in Fig. 19. The time averaged value of drag, for the present computations, is 1.354 which is again in excellent agreement with the value of 1.35 reported in [53].

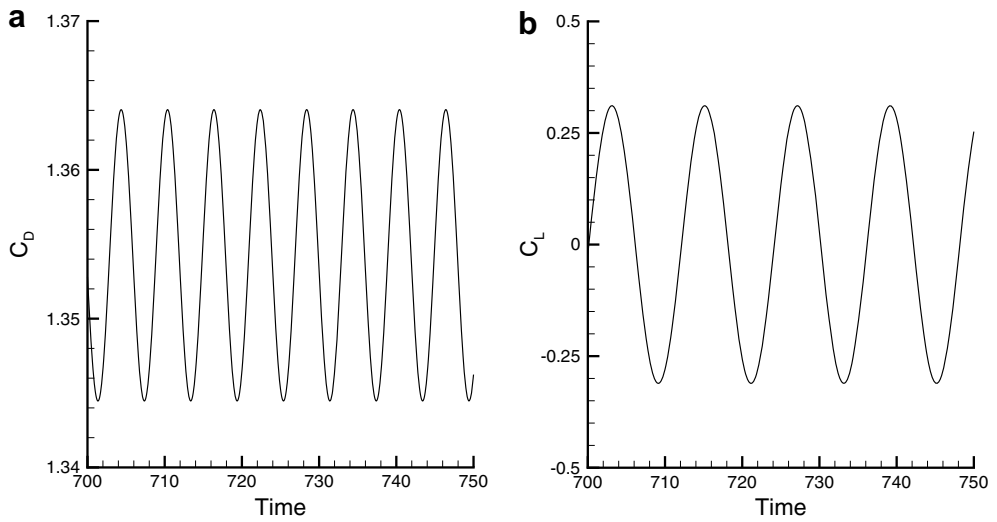


Fig. 18. Variation of: (a) $C_D$ and (b) $C_L$ with time for flow past a circular cylinder at $Re = 100$.

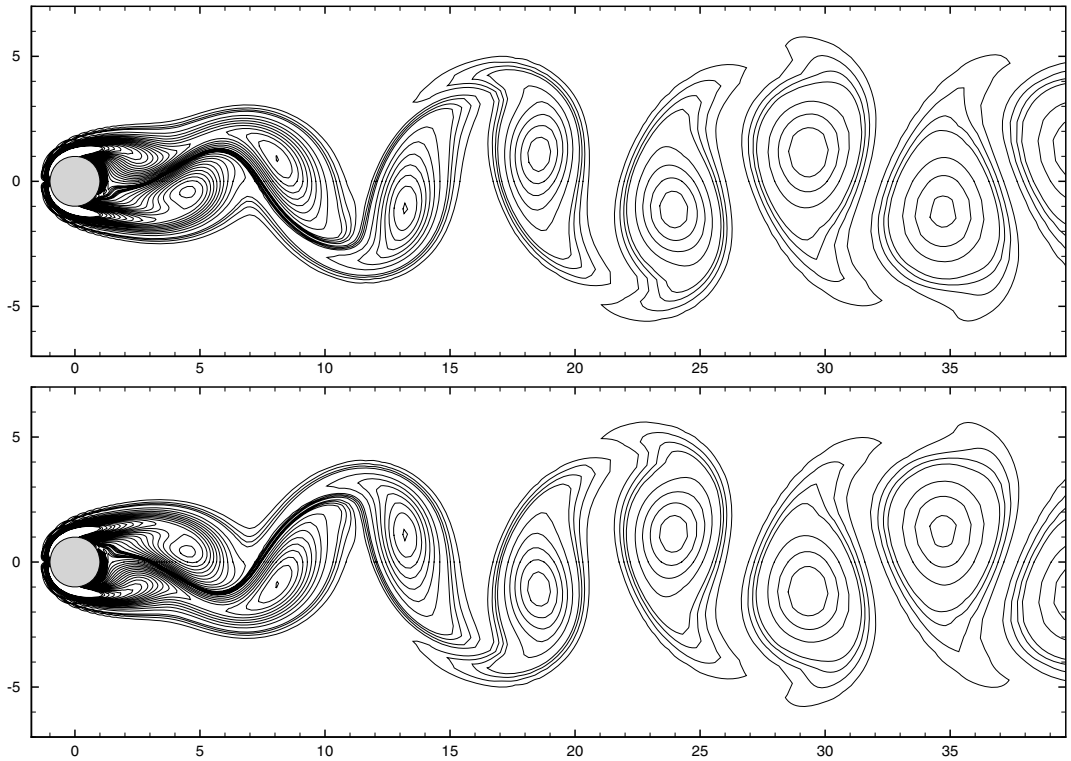


Fig. 19. Iso-vorticity contours for flow at $Re = 100$ obtained using 20th-order compact scheme on a $251 \times 300$ grid at $t = 751.0$ (top) and $t = 757.0$ (bottom). Contour levels are $-2{:}0.1{:}2$ and $-0.1{:}0.025{:}0.1$ excluding 0.

Overall, the results of computations for the incompressible flow show that the high-order compact schemes can be used for computations without any numerical instability problems and provide high-resolution along with high-order of accuracy. The equality between the order of accuracies of the boundary closures and the interior schemes ensures the overall high-order in the entire domain. In this paper we have shown only simple domain computations. Extension to more complex flows in complicated geometries will be presented in future work. In addition, because our schemes for computations and imposition of boundary conditions are not specific to the equations being solved we can also apply these schemes to other formulations like primitive variables with the projection method.

## 6. Conclusions

In this paper compact finite difference schemes over non-uniform grids with very high-orders of accuracy ranging from four to 20 are implemented to solve two-dimensional viscous incompressible flow. Two methods for the numerical solution of Poisson and Helmholtz equations using high-order compact schemes on non-uniform grid are developed. It is shown that the high-order non-uniform grid compact schemes with order of accuracy of up to 20, along with the boundary closures of the same order as the interior, remain stable and give highly accurate results on a non-uniform grid with more grid points clustered at the boundary. The high-order of accuracy and the resolution characteristics of the non-uniform grid compact schemes are verified along with their stability through their application to the linear wave equation and the incompressible flow in the analytical and the singular driven cavity. The high resolution properties of the high-order schemes on non-uniform grids when applied to the incompressible flow are demonstrated through their application to the singular driven cavity at high Reynolds numbers. An extensive comparison of the present numerical results with the previous benchmark solutions for the singular driven cavity flow, convection in a square box and

uniform flow past a circular cylinder establishes the high-order of accuracy and stability of the high-order compact schemes on non-uniform grid.

## Acknowledgments

The first author thanks Professor V.K. Dhir of the MAE Department at UCLA for support during this research. The second and third authors are sponsored by the Air Force Office of Scientific Research, USAF, under AFOSR Grant No. FA 9550-04-1-0029, monitored by Dr. John Schmisseur.

## Appendix A

Here, we present the details of the quadrature rules that are used in this work in order to numerically compute one and two-dimensional integrals. Consider an integral of the form

$$\mathrm{I} = \int_0^1 \int_0^1 f(x,y)\,\mathrm{d}x\,\mathrm{d}y. \tag{A.1}$$

In order to compute this integral numerically using high-order compact finite difference schemes we consider a function $I(x,y)$ given by

$$I(x,y) = \int_0^x \int_0^y f(\eta,\zeta)\,\mathrm{d}\eta\,\mathrm{d}\zeta. \tag{A.2}$$

Then the governing partial differential equation for $I(x,y)$ can be written as

$$\frac{\partial^2 I}{\partial x \partial y} = f(x,y), \quad I(x,0) = I(0,y) = 0. \tag{A.3}$$

Discretization of the above equation using compact finite difference operator relations given by (12) yields

$$Q_1 I Q_2^{\mathrm{T}} = P_1 F P_2^{\mathrm{T}}. \tag{A.4}$$

The above sparse linear system can be solved for discrete value of $I$ at ($x = 1$, $y = 1$) to get a numerical estimate of the integral (A.1). Fig. A.1 shows a plot of error for numerical calculation of (A.1) obtained using

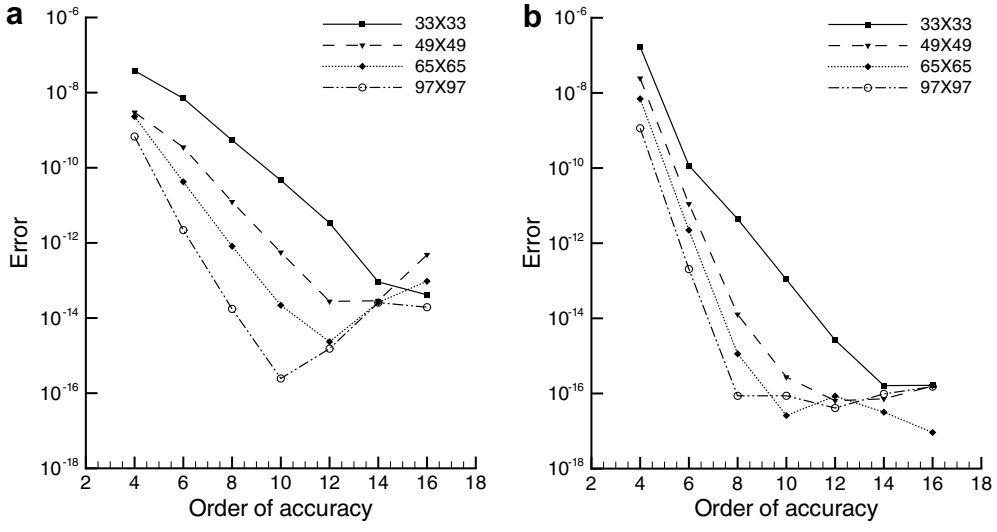


Fig. A.1. Maximum point wise errors for numerical integration using high-order compact schemes on various: (a) uniform and (b) non-uniform grids.

various high-order schemes on uniform and non-uniform grids for $f(x,y) = 2x/(1+x^2+y^2)^2$. We observe excellent agreement between computed and exact result for the value of integral with computations on uniform grid showing some increase in error at very high-orders of accuracy which is related to the Runge phenomena for high-order polynomial interpolation on a uniform grid.

## References


[1] R. Peyret, Spectral Methods for Incompressible Viscous Flow, Springer, New York, 2001.
[2] C. Canuto, M.Y. Hussaini, A. Quarteroni, T.A. Zhang, Spectral Methods in Fluid Dynamics, Springer, New York, 1988.
[3] J.P. Boyd, Chebyshev and Fourier Spectral Methods, second ed., Dover, Mineola, USA, 2000.
[4] D. Kosloff, H. Tal-Ezer, A modified Chebyshev pseudo-spectral method with an O(1/*N*) time step restriction, J. Comput. Phys. 104 (1993) 457.
[5] G.E. Karniadakis, S.J. Sherwin, Spectral/hp Element Methods for CFD, Oxford university press, Oxford, 1999.
[6] R.S. Hirsh, Higher order accurate difference solutions of fluid mechanics problems by a compact differencing technique, J. Comput. Phys. 19 (1975) 90.
[7] S.G. Rubin, P.K. Khosla, Polynomial interpolation methods for viscous flow calculations, J. Comput. Phys. 24 (1977) 217.
[8] S.K. Lele, Compact finite difference schemes with spectral-like resolution, J. Comput. Phys. 103 (1992) 16.
[9] W. E, J.-G. Liu, Essentially compact schemes for unsteady viscous incompressible flows, J. Comput. Phys. 126 (1996) 122.
[10] L. Gamet, F. Ducros, F. Nicoud, T. Poinsot, Compact finite difference schemes on non-uniform meshes. Application to direct numerical simulations of compressible flows, Int. J. Numer. Meth. Fluids 29 (1999) 159.
[11] H.L. Meitz, H.F. Fasel, A compact-difference scheme for the Navier–Stokes equations in velocity-vorticity formulation, J. Comput. Phys. 157 (2000) 371.
[12] K. Bhaganagar, D. Rempfer, J. Lumley, Direct numerical simulation of spatial transition to turbulence using fourth-order vertical velocity second-order vertical velocity formulation, J. Comput. Phys. 180 (2002) 200.
[13] C. Lee, Y. Seo, A new compact spectral scheme for turbulence simulations, J. Comput. Phys. 183 (2002) 438.
[14] S. Nagarajan, S.K. Lele, J.H. Ferziger, A robust high order compact method for large eddy simulation, J. Comput. Phys. 191 (2003) 392.
[15] M. Ben-Artzi, J.P. Croisille, D. Fishelov, S. Trachtenberg, A pure-compact scheme for the streamfunction formulation of Navier–Stokes equations, J. Comput. Phys. 205 (2005) 640.
[16] A. Brüger, B. Gustafsson, P. Lötstedt, J. Nilsson, High order accurate solution of the incompressible Navier–Stokes equations, J. Comput. Phys. 203 (2005) 49.
[17] S. Abide, S. Viazzo, A 2D compact fourth-order projection decomposition, J. Comput. Phys. 206 (2005) 252.
[18] T. Colonius, Modeling artificial boundary conditions for compressible flow, Annu. Rev. Fluid Mech. 36 (2004) 315.
[19] L. Jameson, A wavelet-optimized, very high order adaptive grid and order numerical method, SIAM J. Sci. Comput. 19 (1998) 1980.
[20] X. Zhong, M. Tatineni, High-order non-uniform grid schemes for numerical simulation of hypersonic boundary-layer stability and transition, J. Comput. Phys. 190 (2003) 419.
[21] R.K. Shukla, X. Zhong, Derivation of high-order compact finite difference schemes for non-uniform grid using polynomial interpolation, J. Comput. Phys. 204 (2005) 404.
[22] Z.J. Wang, Spectral (finite) volume method for conservation laws on unstructured grids: basic formulation, J. Comput. Phys. 178 (2002) 210.
[23] Z.J. Wang, Y. Liu, L. Zhang, Spectral (finite) volume method for conservation laws on unstructured grids IV: extension to two-dimensional systems, J. Comput. Phys. 194 (2004) 716.
[24] Y. Sun, Z.J. Wang, Y. Liu, Spectral (finite) volume method for conservation laws on unstructured grids VI: Extension to viscous flow, J. Comput. Phys. 215 (2006) 41.
[25] G. May, A. Jameson, A spectral difference method for the Euler and Navier–Stokes equations on unstructured meshes, AIAA Paper No. 2006-0304, 2006.
[26] G.K. Batchelor, An Introduction to Fluid Dynamics, Cambridge University Press, 1967.
[27] O. Botella, R. Peyret, Benchmark spectral results on the lid-driven cavity flow, Comput. Fluids 27 (1998) 421.
[28] O. Botella, R. Peyret, Computing singular solutions of the Navier–Stokes equations with the Chebyshev collocation method, Int. J. Numer. Meth. Fluids 36 (2001) 125.
[29] U. Ehrenstein, R. Peyret, A Chebyshev collocation method for the Navier–Stokes equations with application to double-diffusive convection, Int. J. Numer. Meth. Fluids 9 (1989) 427.
[30] U. Ghia, K.N. Ghia, C.T. Shin, High-*Re* solutions for incompressible flow using the Navier–Stokes equations and a multigrid method, J. Comput. Phys. 48 (1982) 387.
[31] F. Auteri, L. Quartapelle, Galerkin spectral method for the vorticity and streamfunction equations, J. Comput. Phys. 149 (1999) 306.
[32] F. Auteri, L. Quartapelle, L. Vigevano, Accurate $\omega - \psi$ spectral solution of the singular driven cavity problem, J. Comput. Phys. 180 (2002) 597.
[33] F. Auteri, N. Parolini, L. Quartapelle, Numerical investigation on the stability of singular driven cavity flow, J. Comput. Phys. 183 (2002) 1.
[34] M.M. Gupta, R.P. Manohar, B. Noble, Nature of viscous flows near sharp corners, Comput. Fluids 9 (1981) 379.

[35] W.W. Schultz, N.Y. Lee, J.P. Boyd, Chebyshev pseudospectral method of viscous flows with corner singularities, Journal of scientific computing 4 (1989) 1.
[36] K. Liffman, Comments on a collocation spectral solver for the Helmholtz equation, J. Comput. Phys. 128 (1996) 254.
[37] P.M. Gresho, Incompressible fluid dynamics: some fundamental formulation issues, Annu. Rev. Fluid Mech. 23 (1991) 413.
[38] L. Kleiser, U. Schumann, Treatment of incompressibility and boundary conditions in 3-D numerical spectral simulations of plane channel flows, in: E.H. Hirschel (Ed.), Proceedings of Third GAMM Conference on Numerical Methods in Fluid Mechanics, Vieweg, Braunschweig, 1980, p. 165.
[39] R.K. Madabhushi, S. Balachandar, S.P. Vanka, A divergence-free Chebyshev collocation procedure for incompressible flows with two non-periodic directions, J. Comput. Phys. 105 (1993) 199.
[40] H. Fasel, Investigation of the stability of boundary layers by a finite difference model of the Navier–Stokes equations, J. Fluid Mech. 78 (1976) 355.
[41] O. Daube, Resolution of the 2-D Navier–Stokes equations in velocity-vorticity form by means of an influence matrix, J. Comput. Phys. 103 (1992) 402.
[42] H.J.H. Clercx, A spectral solver for the Navier–Stokes equations in the velocity–vorticity formulation for flows with two nonperiodic directions, J. Comput. Phys. 137 (1997) 186.
[43] J. Trujillo, G.E. Karniadakis, A penalty method for the vorticity–vorticity formulation, J. Comput. Phys. 149 (1999) 32.
[44] J. Xiu, G.E. Karniadakis, A semi-Lagrangian high-order method for Navier–Stokes equations, J. Comput. Phys. 172 (2001) 658.
[45] G. De. Vahl. Davis, Natural convection of air in a square cavity: a benchmark numerical solution, Int. J. Numer. Meth. Fluids 3 (1983) 249.
[46] P.L. Quéré, Accurate solutions to the square thermally driven cavity at high Rayleigh number, Comput. Fluids 20 (1991) 29.
[47] T.M. Shih, C.H. Tan, B.C. Hwang, Effect of grid staggering on numerical schemes, Int. J. Numer. Meth. Fluids 9 (1989) 193.
[48] J.M.C. Pereira, M.H. Kobayashi, J.C.F. Pereira, A fourth-order-accurate finite volume compact method for the incompressible Navier–Stokes solutions, J. Comput. Phys. 167 (2001) 217.
[49] P. Koumoutsakos, A. Leonard, High-resolution simulations of the flow around an impulsively started cylinder using vortex methods, J. Fluid Mech. 296 (1995) 1.
[50] C.R. Anderson, M.C. Reider, A high order explicit method for the computation of flow about a circular cylinder, J. Comput. Phys. 125 (1996) 207.
[51] S. Shankar, A new mesh-free vortex method, Ph.D. Thesis, Florida State University, 1996.
[52] L. Qian, M. Vezza, A vorticity-based method for incompressible unsteady viscous flows, J. Comput. Phys. 172 (2001) 515.
[53] C. Liu, X. Zheng, C.H. Sung, Preconditioned multigrid methods for unsteady incompressible flows, J. Comput. Phys. 139 (1998) 35.
[54] D. Calhoun, A Cartesian grid method for solving the two-dimensional streamfunction–vorticity equations in irregular regions, J. Comput. Phys. 176 (2002) 231.
[55] M.N. Linnick, H.F. Fasel, A high-order immersed interface method for simulating unsteady incompressible flows on irregular domains, J. Comput. Phys. 204 (2005) 157.
[56] S.C.R. Dennis, G. Chang, Numerical solutions for steady flow past a circular cylinder at Reynolds number up to 100, J. Fluid Mech. 42 (1970) 471.
[57] B. Fornberg, A numerical study of steady viscous flow past a circular cylinder, J. Fluid Mech. 98 (1980) 819.
[58] D.J. Tritton, Experiments on the flow past a circular cylinder at low Reynolds numbers, J. Fluid Mech. 6 (1959) 547.
[59] M. Coutanceau, R. Bouard, Experimental determination of the main features of the viscous flow in the wake of a circular cylinder in uniform translation. Part 1. Steady flow, J. Fluid Mech. 79 (1977) 231.